DEPARTAMENT OF
MATERIALS SCIENCE

NOVA SCHOOL OF
SCIENCE & TECHNOLOGY

Ivan Miranda Santos

BSc in Materials Science Engineering

Light Management in Crystalline Silicon Solar Cells with Photonic Nanocoatings

MASTER IN MATERIALS SCIENCE ENGINEERING

NOVA University Lisbon

October, 2022

DEPARTAMENT OF
MATERIALS SCIENCE

Light Management in Crystalline Silicon Solar Cells with Photonic Nanocoatings

IVAN MIRANDA SANTOS

BSc in Materials Science Engineering

Adviser: Manuel João de Moura Dias Mendes
Assistant Professor, NOVA University Lisbon

Co-advisers: Ana Isabel Machado Mouquinho
Post-doctoral researcher, NOVA University Lisbon

Examination Committee:

Chair: Rui Alberto Garção Barreira do Nascimento Igreja
Assistant Professor, NOVA University Lisbon

Rapporteurs: José Almeida Silva
Senior Researcher, Dom Luiz Institute, Faculty of Sciences of the University of Lisbon

Adviser: Manuel João Moura Dias Mendes
Assistant Professor, NOVA University Lisbon

Members: Ana Isabel Machado Mouquinho
Post-doctoral researcher, NOVA University Lisbon

MASTER IN MATERIALS SCIENCE ENGINEERING

NOVA University Lisbon
October, 2022

Light Management in Crystalline Silicon Solar Cells with Photonic Nanocoatings

To you, my love.

Acknowledgements

It is with great pride and nostalgia that I leave my sincerest appreciations to all referred below, for marking this journey somehow in such a unique manner.

To Sónia Soares, Prof. Alexandre Velhinho, Prof. João Borges, Prof. Rodrigo Martins, Prof. Elvira Fortunato, Alexandra Gonçalves and Mafalda Gonçalves, that allowed for such a simple process. I also give my appreciation to CENIMAT|i3N, CEMOP and DCM (as their behind-the-scenes members), for allowing me to proceed freely with my work. To Dr. Maria Brites (LNEG), Dr. Sandra Gago (DQ) for the availability, help and support. To Dr. Valentin Mihailetchi, Dr. Eckard Wefringhaus and Dr. Florian Buchholz (ISC Konstanz, Germany) I leave my professional and personal appreciation for the high-quality samples and given support.

To the members of the group that I had the luck to work with, thank you: Pedro Centeno, Deneb Menda, António Vicente, Jenny Boane, Miguel Alexandre, Tiago Mateus. Thank you for allowing me to learn so much with each one of you, for your humility, memorable times and conversations, but mainly for making this journey so enjoyable. I also want to thank my co-adviser, Ana Mouquinho. I believe that, even with such constrictions, your support and guidance helped me so deeply. I cannot talk about guidance without referring my adviser: Prof. Manuel Mandes. I personally want to thank you for giving me the chance to embrace this world on my own terms. For your advice and readiness that I appreciated so much. For becoming an "unconscious" professional role model, that led me to push myself in every single detail, not only to drive this group even further, but also to travel in a high-level professional career.

Para vocês, pais e irmão, obrigado. Espero que esteja seja uma prova de que todo o esforço que tiveram a educar-me, e na adaptação a estes últimos anos valeram realmente a pena. Para vocês, espero que isto não simbolize apenas um motivo de orgulho, mas sobretudo um voto de confiança para o percurso que espero e farei por ter, neste mundo que pouco conhecem, mas que adoro.

To you, my love… Thank you for all the support and concern, all the memorable conversations, including those when I tried to explain my work and the effort that you putted to understand it. Thank you for understanding the time that I did not spend with you. I tried my best to give you all that you deserve. Thank you for removing the heavy weights that I carried. For being patient and humble. Thank you for lighting up the best part of me: you. Thank you for your golden heart. I love you. Unconditionally.

To my future self, may this be proof of your wisdom to distinguish the things that you can and cannot change.

Abstract

Light management via photonic nanostructured coatings sustains a broad set of possible solar energy conversion enhancements, alternatively to conventional texturing processes that deteriorate solar cells (SCs) electrical transport through charge carrier recombination losses. These coatings, composed of high-refractive index materials structured at the sunlight wavelengths scale, can improve SCs efficiency, avoiding surface texturing processes while still allowing high-performance light trapping (LT).

Here, through a highly scalable colloidal lithography methodology, proposed titanium dioxide (TiO_2) nanovoid coatings were patterned on conventional (250 μm) and thin (90 μm) flat crystalline silicon (c-Si) wafers. These nanostructured coatings were also applied on textured (130 μm c-Si absorber), etched (140 μm) and flat (740 μm) c-Si interdigitated back contact solar cells (IBCSCs).

The subsequent broadband absorption amplification was owing to the combined effects of (1) light scattering in near-infrared (NIR) wavelengths and (2) broad anti-reflection. With coated 250 μm c-Si wafers, a photocurrent density (J_{ph}) of 36.6 mA/cm² was determined by absorption spectrum integration between 350 and 1200 nm. Approximately 84 % of the maximum theoretical J_{ph} Lambertian LT limit is here attained with 669 and 693 nm of TiO_2 thin photonic nanostructured coatings, respectively with the considered conventional and thin c-Si wafers.

When integrated into test devices, outstanding optical improvements are attained without diminishing the original electrical performance by applying coatings with TiO_2 thicknesses ≥ 545 nm. Unprecedent ~30 % of efficiency enhancement and 31.9 mA/cm² of short-circuit current density (J_{sc}) are demonstrated with etched IBCSCs coated with 885 nm of TiO_2 nanostructured coating. Additionally, unmatched optical angular acceptance is shown: 63 % of efficiency and 68 % of J_{sc} enhancements are respectively exhibited with 545 and 885 nm of TiO_2 coatings for 80° of light incidence angle. Hence, with straightforward near-future integration in the established industry, a highly promising path for c-Si photovoltaic improvement is entailed.

Keywords: Photovoltaics, Light Management, Colloidal Lithography, Crystalline Silicon Solar Cells, Photonic Nanostructured Coatings

Resumo

A gestão de luz mediante o uso de revestimentos nanoestruturados fotónicos sustenta um vasto leque de possíveis melhorias de conversão de energia solar, alternativamente a processos convencionais de texturização que deterioram o transporte eléctrico de células solares (CSs). Estes, compostos por materiais de elevado índice de refracção, podem elevar a eficiência de CSs, evitando texturizações enquanto possibilitam a captura de luz de elevado desempenho.

Matrizes de nanocavidades de dióxido de titânio (TiO_2) foram padronizadas por uma metodologia altamente escalável de litografia coloidal em bolachas de silício cristalino (c-Si) plano convencionais (250 μm) e finas (90 μm) e em CSs de contactos posteriores interdigitados (IBCSCs) texturizadas (130 μm c-Si), erodidas (140 μm) e planas (740 μm).

A subsequente amplificação extensa da absorção deve-se à combinação dos seguintes efeitos: (1) dispersão de luz para comprimentos de onda do infravermelho próximo e (2) antirreflexão ampla. Com bolachas de c-Si convencionais, uma densidade de fotocorrente (J_{ph}) de 36.6 mA/cm² determinada pela integração da absortância (350-1200 nm) foi conseguida. Aproximadamente 84 % do limite máximo teórico Lambertiano foi atingido com bolachas convencionais e finas revestidas com 792 e 693 nm de TiO_2 nanoestruturado, respetivamente.

Quando integrados em dispositivos de teste, a aplicação desses revestimentos com espessuras de $TiO_2 \geq 545$ nm conduziu a uma melhoria ótica substancial sem diminuir o desempenho elétrico original. Um aumento de ~30 % de eficiência e 31,9 mA/cm² de densidade de corrente de curto-circuito (J_{sc}) são apresentados com IBCSCs revestidas com 885 nm de TiO_2 nanoestruturado. É ainda demonstrada uma aceitação angular ótica incomparável: ganhos de 63 % de eficiência e 68 % de J_{sc}, respetivamente com revestimentos de 545 e 885 nm de TiO_2 nanoestruturado para um ângulo de luz incidente de 80°. Assim, com uma integração num futuro próximo na indústria, um caminho promissor para a evolução fotovoltaica em c-Si é implicado.

Palavras-chave: Fotovoltaico, Gestão de Luz, Células Solares de Silício Cristalino, Litografia Coloidal, Nanofotónica, Revestimentos Fotónicos Nanoestruturados

Contents

List of Figures

List of tables

Symbols and Abbreviations

°	Degrees
G	Generation Rate
k	Refractive Index Imaginary Part
n	Refractive Index Real Part
$E_{\langle \mathrm{Abs} \rangle}$	Average Absorption Enhancement
$E_{\mathrm{J_{ph}}}$	Photocurrent Density Enhancement
FoM_{op}	Optical Figure-of-Merit
J_{ph}	Photocurrent Density
J_{sc}	Short-Circuit Current Density
V_{oc}	Open Circuit Voltage
t_{RIE}	Reactive Ion Etching time
μL	microlitre
μm	micrometre
A	ampers
AFM	Atomic Force Microscopy
Ag	Silver
Ar	Argon
ARC	Anti-Reflection Coating
a-Si	Amorphous Silicon
A_T	Total Absorptance
AZO	Aluminium-doped Zinc Oxide
CF_4	Carbon Tetrafluoride
CL	Colloidal Lithography
cm	centimetre
cm^2	Square centimetre
c-Si	Crystalline Silicon
DI	Deionized Water
eIBCSC	Etched Interdigitated Back Contact Solar Cell
EQE	External Quantum Efficiency
EtOH	Ethanol

FF	Fill Factor
FFT	Fast-Fourier Transform
fIBCSC	Flat Interdigitated Back Contact Solar Cell
IBCSC	Interdigitated Back Contact Solar Cell
in	Inches
ITO	Indium Tin Oxide
IZO	Indium Zinc Oxide
LB	Langmuir-Blodgett
LIA	Light Incidence Angle
LT	Light Trapping
m	metre
m²	Square metre
mA	milliampers
mbar	millibar
min	minute
ml	millilitre
mm	millimetre
mTorr	millitorr
Mo	Molybdenum
NIR	Near-Infrared
nm	nanometre
O_2	Oxygen
PCE	Power Conversion Efficiency
PET	Polyethylene Terephthalate
PS	Polystyrene
PSC	Perovskite Solar Cell
PV	Photovoltaic
PVD	Physical Vapor Deposition
R_D	Diffuse Reflectance
RF	Radio-Frequency
RIE	Reactive Ion Etching
R_T	Total Reflectance
s	Second
SC	Solar Cell

sccm	Standard cubic centimeters per minute
SEM	Scanning Electron Microscopy
Si_3N_4	Silicon Nitride
TCO	Transparent Conducting Oxide
T_D	Diffuse Transmittance
TFSC	Thin-Film Solar Cell
tIBCSC	Textured Interdigitated Back Contact Solar Cell
TiO_2	Titanium Dioxide
T_T	Total Transmittance
TW	Terawatt
UV	Ultraviolet
Vis	Visible
W	Watt
ZnO	Zinc Oxide

Motivation and Objectives

The worldwide energy demand and consequent interest in renewable green energy sources have grown intensively for the past 20 years. Among them, solar energy held the majority of the worldwide electrical production capacity, claiming a share of 56 % and surpassing the 1 TW threshold of total global installed solar capacity yearly this year.[1,2] Unlike hydro or wind energy, solar does not require large infrastructures for electricity production due to the relatively easy-to-handle and install photovoltaic (PV) devices, which strengthens their consistent market leadership.[3–7]

The PV market is governed by thick crystalline silicon (c-Si) wafer solar cells, whose efficiency reaches up to ~26 %.[2,8] Despite their high longevity (~20 years), their applications are narrowed, as they are heavy, thick, and lack mechanical flexibility.[9] In contrast, thin-film solar cells (TFSCs) assure mechanical flexibility and low manufacturing costs due to their low thickness, varying from a few nanometers up to a micron. They are easy-to-handle, lightweight, and use the least material. This attracts cost-effective production processes, such as roll-to-roll, which unlocks a wide range of consumer-oriented applications.[2,8,9] However, light intensity in a material decreases exponentially (hence absorption), according to Lambert-Beer law. Therefore, TFSCs typically present lower efficiency (~15 %)[10] due to their lower thickness and, so, material usage, with respect to conventional thicker solar cells.[6,8] As such, further technological conversion efficiency enhancements are necessary to enhance light absorption while maintaining the low thickness of these devices to implement them on the market, assuring global energy PV devices with a high-efficiency goal and minimum material usage.[11,12]

To that end, structures composed of high-refractive index materials are one of the preferred solutions for light trapping (LT). Employing these, it is possible to maintain or even reduce their absorber thickness, while allowing mechanical bendability without deteriorating solar cells' performance.[13–15] Due to their wave-optics range dimensions, these structures can be fabricated by a high-resolution soft-lithography procedure known as colloidal lithography (CL). Beyond allowing a low-cost patterning of almost any material, it is suitable for PV industry production process requirements (as roll-to-roll)[2] that are assured throughout the work presented here.

Contrastingly, conventional LT methods rely on optimized texturing processes (i.e., textured rear/front surfaces) to increase photons' path length within the absorber,

resulting in absorption enhancements in c-Si wafers close to the so-called $4n^2$ classical absorption limit.[10,16] Oppositely to the here-designed LT coatings, texturing processes lead to cells' electrical performance deterioration owing to the increase in charge carrier trapping and recombination caused by, in turn, the increase of defect density (see Figure 1).[10]

For the first time, this work aims for the experimental wavelength-scale structured coating application directly on thin and conventional (90 and 250 μm, respectively) c-Si wafers and on etched (140 μm c-Si absorber thickness) interdigitated back-contact solar cells (IBCSCs), trough CL process, and their visual, optical and electrical characterization. A complementary study on thick randomly textured (130 μm) or flat (740 μm) IBCSCs is also made. The final results are compared with the most recent and comparative literature, to the authors' knowledge. As so, with a hoped increase in optical and/or electrical performance (hence absorption and efficiency) and assuring scalability with the CL method, a potential insertion of this simple and versatile novel approach on PV commercial solar cells production methods is projected in a near-future.

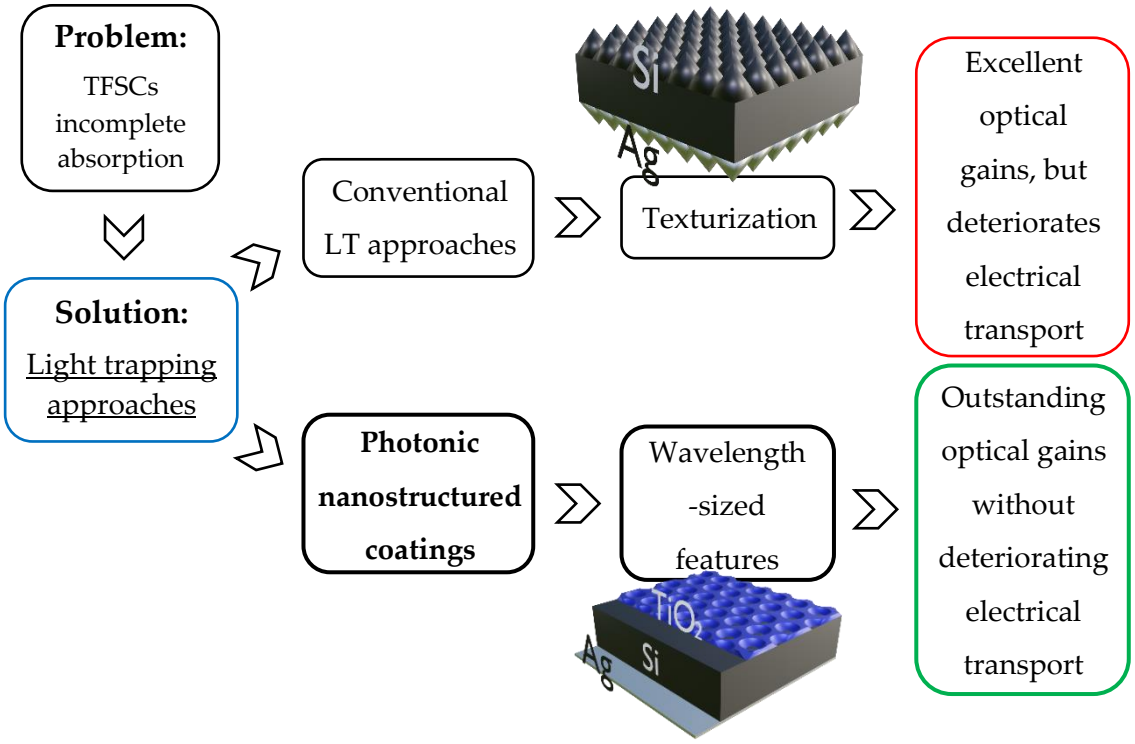

Figure 1. Light trapping (LT) approaches are the preferred solutions to solve the solar cells' incomplete absorption of thin-film solar cells (TFSCs). Instead of conventional texturing processes, LT wavelength-sized features (see bottom sketch) lead to remarkable optical enhancements without deteriorating solar cells' electrical performance.

1 INTRODUCTION

1.1 Light Trapping Approaches

Among potentially industrial scalable technologies in green energy conversion, thin-film solar cells (TFSCs) are the most promising ones, assuring the least material usage and, thus, flexibility, which leads to highly scalable production methods and a broad range of applications.[10,17–19] Still, their typical considerably low efficiency constitutes an obstacle to their worldwide market growth. Thus, further efficiency improvements must be accomplished.

To that end, conventional light trapping (LT) approaches target light reflection and transmission reduction, and hence, light absorption increase within the solar cells' absorber layer.[7,8] These act mainly on a narrow range (short-wavelength Ultraviolet-Visible, UV-Vis, photons) through refractive index matching, attained with front anti-reflection coatings (ARCs) application, which diminishes front reflection.[20] They also take advantage of rear reflectors, allowing for a more horizontal optical path of the long-wavelength photons (near-infrared, NIR) owing to internal reflection. Thus, greater distances than the absorber thickness are traveled, which enhances their absorption probability.[21] In turn, that allows for the decrease of the absorber layer thickness, which diminishes the cells' production cost, enabling optically thicker but physically thinner high-performance solar cells.[10] Conventional LT methods include texturing, which boosts geometric antireflection and enables light scattering effects. However, the resultant micron-scale textures do not follow the absorber thickness reduction, and defect density is enhanced through texturing. Subsequently, cells' electrical performance is deteriorated by charge carriers trapping or recombination.[7,15]

On the other hand, wavelength-scale high-refractive index structures are identified as one of the most desirable LT approaches for front surface integration on photovoltaic devices. They not only enhance high-performance light trapping (hence absorption) in thin-film photovoltaic (PV) devices but also maintain or even improve their electrical performance, avoiding texturing processes.[22–24] This is attributable to (1) diminishing of light reflection at short wavelengths (UV-Vis) by the varying cross-sectional shape of these structures; (2) not only but also consequent gradual effective refractive index matching with the high-refractive index absorber; (3) forward light scattering of NIR photons, which is owing to the path length increase of the propagating far-field and to the intense near-field generated underneath the designed structures.[10,23]

These simulated LT structures comprise two specific vertical arrays of aligned semispheroidal elements separated in a flat layer of TiO_2 or transparent conductive oxide (TCO), which are represented in Figure 1.1:[13,20]

- *Domes array* – TiO_2 half-spheroids, as depicted in Figure 1.1A, separated in a flat TCO layer, Aluminium-doped Zinc Oxide (AZO), e.g.,
- *Voids array* – Semispheroidal cavities in a TiO_2 or TCO layer, depicted in Figure 1.1B.

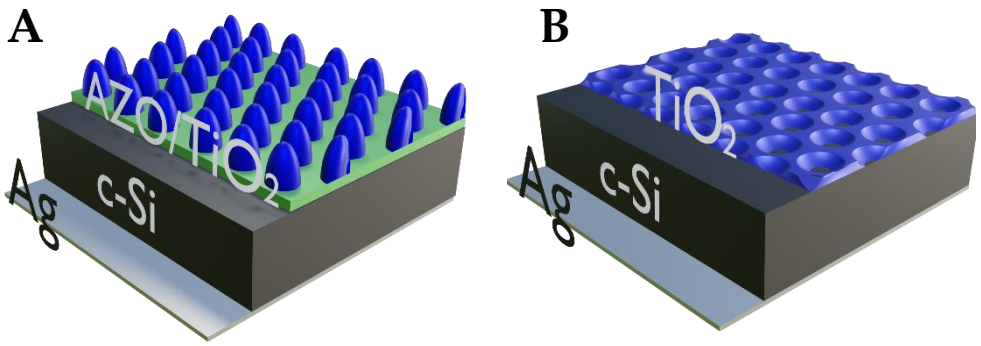

Figure 1.1. LT designs sketches (**A**) domes and (**B**) voids geometry patterned on a c-Si absorber layer, e.g., as they can be virtually applied on any surface. These are composed by titanium dioxide, separated by an aluminum-doped zinc oxide (AZO) in the domes design.

Titanium dioxide has been preferentially chosen as constituting material due to its refractive index relatively high-real part (n) and low imaginary part (k) in the Vis-NIR range.[10] The first one favors antireflection since it provides a gradually varying effective refractive index matching to the incident light, as referred to above, and scattering effects observed in NIR wavelengths.[25] In turn, the second implies negligible parasitic absorption, i.e., undesired absorption in singular or several other layers than in the absorber one.[26,27] Nonetheless, TiO_2 is a dielectric with a low electrical conductivity that encumbers its integration and functionality as PV devices' front TCO contact layer.[10] Consequently, TCO materials can be preferred for such applications due to their higher conductivity, despite their lower n and higher k, as ZnO-based TCOs (e.g., Aluminum-doped Zinc Oxide, AZO). Additionally, they are abundant, nontoxic, and present excellent transparency.[10] Although these AZO front structures present substantial photocurrent density (J_{ph}) enhancements relative to the standard ARCs,[15,23] they are still lower than those attained with TiO_2 due to the following: [10] lower n of AZO (n~1.8-2), relative to respective TiO_2 (n~2.5-2.7), is more separated that the ideal one (n_{Si}~4), leading to worse impedance matching of sunlight and disfavoring light in-coupling; lastly, the higher k leads to higher parasitic losses in the NIR band, when compared to the same structures of TiO_2.

In the context of cell volume light absorption distribution reported in previous simulation works, the generation rate (*G*) profiles, which evaluate the carriers' generation in the structures' cross-sectional plane, are distinct between arrays. The profiles attained with TiO_2 domes structures expose more intense "hot spots" located beneath the domes.[14] This is attributable to the microlenses effect of their round shape that focuses the light in a confined photonic jet near-field region.[10] In turn, the voids array lead not only to less intense underneath "hot spots" but also to a more delocalized light absorption distributed along the active layer volume, acting as a diffraction grating that enhance the path length of NIR photons.[23] These elements do not present sharp edges or corners, as other reported LT features.[28] Hence, the generation of near-fields localized in the structures that, in turn, tend to dissipate energy as heat, is prevented.[10] Besides, these presented curved structures are less sensitive to the light incidence angle, which becomes relevant to the applicability of non-tracking devices, particularly on flexible substrates.[14] Lastly, their integration is facilitated by the incorporation as the last processing step on a photovoltaic device with a substrate-type layer configuration without diminishing the flexibility of TFSCs.[29]

Both simulated features present similar but yet distinct absorption spectra for the same constituting material (TiO_2). The more delocalized scattered-field is more beneficial for thicker absorbers, particularly in NIR wavelengths, as with the simulated 300-nm a-Si and 1500-nm c-Si. In this case, the voids array leads to greater J_{ph} enhancements (27 and 48 %, respectively) compared to those offered by the domes' array (24 and 44 %, respectively).[10,23] In turn, the optimized domes array is preferential for ultra-thin absorbers, as for simulated 100-nm a-Si, leading to higher J_{ph} enhancement (37 %) than with the voids array (34 %). This is due to the microlenses effect in NIR of the first, that concentrates the highest amount of photons as possible in such low volume.[14,23]

1.2 Colloidal Lithography

Several methods are capable of producing the referred nanostructured coatings.[30–33] Among them, colloidal lithography (CL) allows processing simplicity, low cost, and precise nano-structuration over large areas.[10,34] It follows at low temperatures (< 100 °C), allowing the usage of temperature-sensitive materials (e.g., perovskite) and the patterning of a broad range of materials, which is more convenient for large-scale fabrication. Moreover, its typical minimum resolution range (50-200 nm) is comparable to that of considerably more expensive state-of-the-art hard-lithography methods.[2,35,36]

Both voids and domes LT arrays can be produced by employing one of the two methods depicted in Figure 1.2.[10] As illustrated, both methods involve four main steps:

(1) microspheres colloidal self-assembly into a well-ordered close-packed monoarray via wet-coating (e.g., Doctor-Blade or Langmuir-Blodgett, LB), which covers the substrates surface; (2) colloidal mask shaping through selective reactive ion etching (RIE); material deposition through (3) physical vapor deposition (PVD) method, e.g., radio-frequency (RF) sputtering; and, lastly, (4) etched colloids lift-off, usually by bath sonication in an appropriate solvent.[2,10] The main differences between both methods depicted in Figure 1.2 are the first two stages. As represented in method 1, the highly selective reactive ion etching only acts on the colloidal particles, defining the mask to the subsequent void-like design. In method 2, the less-selective RIE also affects the underlying layer, resulting in dome-like features.[2] After the material infiltration through PVD, a lift-off procedure removes the colloidal particles without acting on the photonic structure array. On such occasions, chemical removal, thermal annealing[37], and oxygen plasma treatments[38] can be performed to remove the polymeric residues.

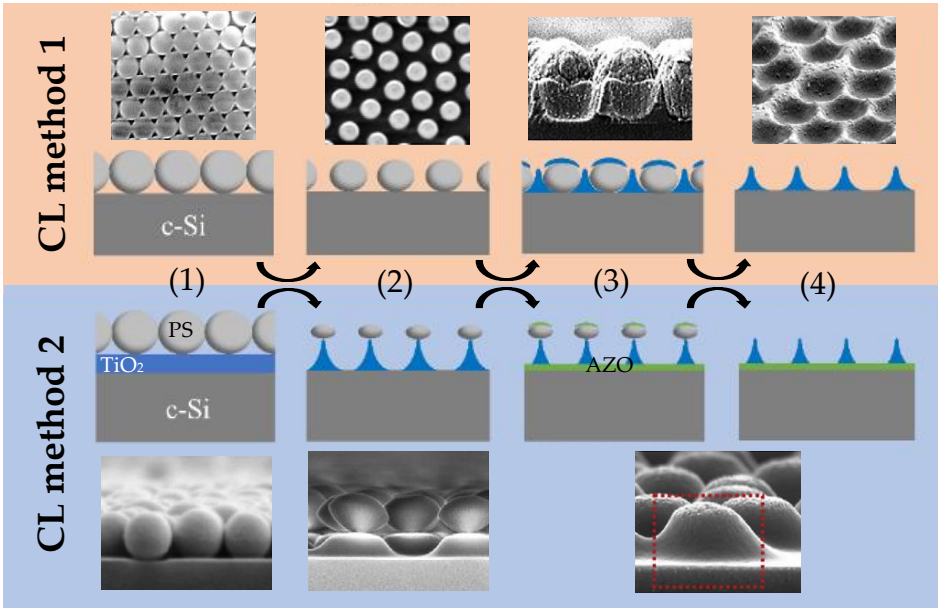

Figure 1.2. Distinct colloidal lithography (CL) methodologies to design respective photonic microstructures: method 1 results in semispheroidal void-like features; method 2 results in dome-like front features. Scanning Electron Microscopy (SEM) images after each step are presented. Adapted from ref.[2]

1.3 Silicon and Perovskite-based Solar Cells Improved with LT Structures and CL compatibility

O. Sanchez-Sobrado et al.[7,15,24] started by introducing a-Si TFSCs with nanophotonic front configurations that were engineered via CL using LB-transferred colloidal masks, reaching up to ~53 % and ~52 % of J_{ph} and efficiency enhancement, respectively, with optimized flat indium zinc oxide (IZO) as front TCO with a thickness of 190 nm, at ± 70°

of incidence angle, and ~52 % also in efficiency enhancement at $\pm 40°$ with 30 nm ultrathin thickness and 700-800 nm of LT voids thickness.

So far, although promising and compatible with CL, the aforementioned light trapping patterning procedures depicted in Figure 1.2 should be applied on top of planar solar cells. However, the degradation of the underneath and sensitive materials (e.g., perovskite) is imposed, since these must be immersed or coated with aqueous solutions as required by any CL method.[2] Recently, Haque et al.[13] proposed an industrially attractive methodology, where a perovskite deposition is made on already nanostructured substrates. Consequently, flexibility was still attained for ultra-thin (300 nm) and conventional (500 nm) thicknesses of perovskite absorber. Moreover, the simulated J_{ph} increase of ~23 % in superstrate cell configuration, where light enters the device from the substrate lateral, and ~24 % in inverted substrate-type configuration, where light enters from the films' side, were stated. In addition to superior broadband absorption attained with the simulated LT domes, several other important advantages arise from the use of these wave-optical structures:[10] (1) material compatibility, since titanium dioxide is typically used as electron transport material in the state-of-the-art, which can be coated with TCO as front electrode; (2) electrical preservation, through roughness formation (thus recombination due to induced defect density) prevention, which is specifically beneficial for perovskite solar cells (PSCs), since surface defects lead to their primary recombination mechanism; (3) the front coated titanium dioxide light trapping structures act as UV-blocking layers, protecting the sensitive perovskite absorber layer from degradation while it enhances light absorption closer to the bandgap; and, lastly, (4) the presented photocurrent enhancement enables flexibility and cost reduction, which confers its broad applicability.

More recently, Boane et al.[8] presented an innovative approach of photonic transparent electrodes, where indium zinc oxide (IZO) on poly(ethylene terephthalate) (PET) substrates coated with indium tin oxide (ITO) were patterned through CL. A substantial sheet resistance reduction (~30 %) was attained, providing electrical benefits due to contact conductance improvement. With this, a novel class of bendable photonic transparent electrodes applicable to a wide range of optoelectronic applications, like as front contacts of TFSCs (with perovskite as the active layer, for instance), is proposed. Yet, several research fronts are envisaged, like smaller LT structures, as simulated by Haque et al.[13], or applying microstructured ITO coatings instead of IZO, to achieve the highest efficiencies possible with these novel high-performance technologies.[9]

2 EXPERIMENTAL

2.1 Samples preparation and characterization

2.1.1 *Preparation*

Conventional (250 ± 25) μm and **thin** (90 ± 10) μm **crystalline silicon** (c-Si) **double-side polished wafers** with respective diameters of 2 and 4 inches from *Siltronix* were cutted and submitted to 15 minutes of ultrasonication in isopropyl alcohol. After water and ethanol rinsing, these were dried under a nitrogen flow.

Textured IBC solar cells (130 μm c-Si absorber, 12.5 × 12.5 cm^2) were submitted to laser cut (Laser System PLS6MW) resulting in 12.5 × 4.2 cm^2 interdigitated back contact solar cells (IBCSCs). These and **thick etched** (140 μm c-Si absorber) and **flat** (740 μm c-Si absorber) **IBCSCs** from ISC Konstanz (Germany) with 2.1 × 2.1 cm^2 were also prepared as described above.

2.2 Colloidal Lithography

The wet-coating methodology here used to engineer the photonic nanostructured coatings is explained below, which is similar to related works[8,15,24].

2.2.1 *Polystyrene suspension preparation and Langmuir-Blodgett*

A 10 % colloidal suspension of polystyrene (PS) spheres with a diameter of (1.30 ± 0.03) μm was purchased from Microparticles *GmbH*. To ensure the spheres' floatation in the air-liquid interface, a similar method presented by Akinoglu et al.[39] was performed (Appendix A, section 1). A Biolin Scientific KSV NIMA controllable Langmuir-Blodgett (LB) setup was used to fabricate PS 2D colloidal masks, following the methodology presented in Appendix A, section 2.

2.2.2 *Colloidal mask shaping and TiO_2 infiltration*

Using a Trion Phantom 3 reactive ion etcher, the spheres' geometry was tuned by O_2 reactive ion etching (RIE) exposure, with the conditions listed in Table SA1 (first row, Appendix A, section 3). Titanium dioxide (TiO_2) was deposited via radio frequency magnetron sputtering (see Table SA2, Appendix A, section 3). Glasses with 2.5 × 2.5 cm^2 were submitted to every deposition to evaluate the resultant TiO_2 thickness by simulation, as described below (sub-subsection 2.3.2).

2.2.3 *Colloidal mask lift-off*

An Ar/CF_4 mixture RIE (see Table SA1, second row, Appendix 3, section 3) was employed to remove the top capping layer of TiO_2, exposing the PS spheroids, followed by the chemical dissolution of those spheroids in a toluene sonication bath for 1 hour.

2.3 Photonic nanostructured coatings characterization

2.3.1 *Morphological and topographical characterization*

Top/tilted views taken by Scanning Electron Microscopy (SEM) using SEM Hitachi Regulus SU8220 were used to confirm the PS spheres removal and to characterize the fabricated nanostructures morphology. These were processed to obtain Fast Fourier Transform images and Voronoi diagrams. The topography of coated conventional c-Si wafers was revealed by Atomic Force Microscopy (AFM) using Asylum MFP3D.

2.3.2 *Optical characterization*

Using a scanning spectrophotometer (PERKIN ELMER Lambda 950), the total (T_T) and diffuse (T_D) transmittance and also total (R_T) and diffuse (R_D) reflectance spectra of the prepared wafers and IBCSCs were measured prior and after the CL procedures in the respective intervals: 350-1400 nm and 350-1200 nm. The total absorptance (A_T) was determined using the following formula: $A_T(\,\%) = 100\,\% - T_T(\%) - R_T(\%)$. The TiO_2 thicknesses were determined by fitting the measured T_T spectra of the deposited films to analytically simulated ones for an arbitrary number of 1D stacked flat layers (see Tables SA4 and SA5 for simulated thicknesses), using the Scattering Matrix Method (*https://bit.ly/3RU28J1*), as exemplified in Figure SA1 (Appendix A, section 3).

2.3.3 *Photovoltaic response*

The textured and etched IBCSCs I-V curves measurements were performed using a Sun Simulator (SPI 240A) and LED Sun Simulator (Oriel VeraSol LSH-7520), respectively. Angular measurements were taken by adapting the sample holder with a goniometer. Respective external quantum efficiency (EQE) measurements were performed using a Newport QuantX-300 system, between 350-1200 nm with a 10 nm wavelength step. All of these measurements were performed prior and after the CL wet-coating processes.

2.4 Ag rear mirror and wafers optical re-characterization

Ag rear mirrors (~300 nm Ag) were deposited via resistive thermal evaporation (details in Table SA3, Appendix A, section 3) on the prepared c-Si wafers. The deposited Ag thicknesses were confirmed by profilometry, using a Dektak 3 Profilometer. After the Ag back mirror deposition, only the R_T and R_D were re-measured, where A_T was calculated neglecting transmittance.

3

RESULTS AND DISCUSSION

In this chapter, the various contributions of the here-designed photonic coatings are discussed regarding their morphology, topography and optical impacts when applied on thick conventional (250 μm) or thin (90 μm) flat crystalline silicon (c-Si) wafers.

Interdigitated back contact solar cells (IBCSCs) are the most suitable for the application of these coatings on test devices, since their front implementation through colloidal lithography (CL) processes should maintain or improve their original electrical performance, as stated in related literature.[15] These were designed on thick etched (140 μm) IBCSCs, whose electrical performance is also addressed. Preliminary results on textured (130 μm c-Si thickness, originally covered with optimized anti-reflection coating) and flat (740 μm) IBCSCs are presented in Appendix B, respectively, in subsections 2.4 and 2.5. The applied CL method in Figure 1.2A will be detailed first, as it gives rise to the nanostructured coatings here engineered. The voids array design was the only applied, since it is the most suitable regarding the different referred thicknesses (90-740 μm).[10,15,24]

3.1 Colloidal Lithography

3.1.1 Suspension preparation

The earlier introduced CL process starts with the deposition of a colloidal monolayer on the substrate, which acts as a mask that shapes the subsequently infiltrated material. Previously, the mask, ideally composed of a hexagonally ordered monoarray of polystyrene (PS) spheres, was completely transferred by Langmuir-Blodgett (LB) from an air-liquid interface to the substrate. To that end, the floatation of those spheres must be verified. However, the original 10 % colloidal suspension of non-functionalized PS spheres with ~1.3 μm diameter used in this work contained water-soluble surfactants and salts, which lead to their immersion in the liquid, as they reduce the spheres' surface tension, turning it whitish.[40] increase possible approach to enable their floatation and consequent self-assembly is detailed in Appendix A, section 1, and was commonly applied in this work. With this, a similar functionalization process (depicted in Figure 3.1) to that described in literature should occur:[41,42] a) short sulfonation reaction, where negatively charged PS spheres with adsorbed $-SO_3H$ groups are obtained. The low used percentage of sulfuric acid (0.1 %) is sufficient to remove the tensioactivity provided by

the surfactants and salts; b) the adsorption of the monomer (styrene) to the PS charged spheres. Consequently, these spheres' surface tension is increased, allowing their floatation in water. It is worth noting that this only constitutes a plausible first explanation for the here occurred, as the presented literature validates it. However, further analysis should be considered, such as Fourier-transform infrared spectroscopy, which could be used to determine the constituting molecular groups, or x-ray photoelectron spectroscopy to analyze the PS spheres' surface chemical composition.[43]

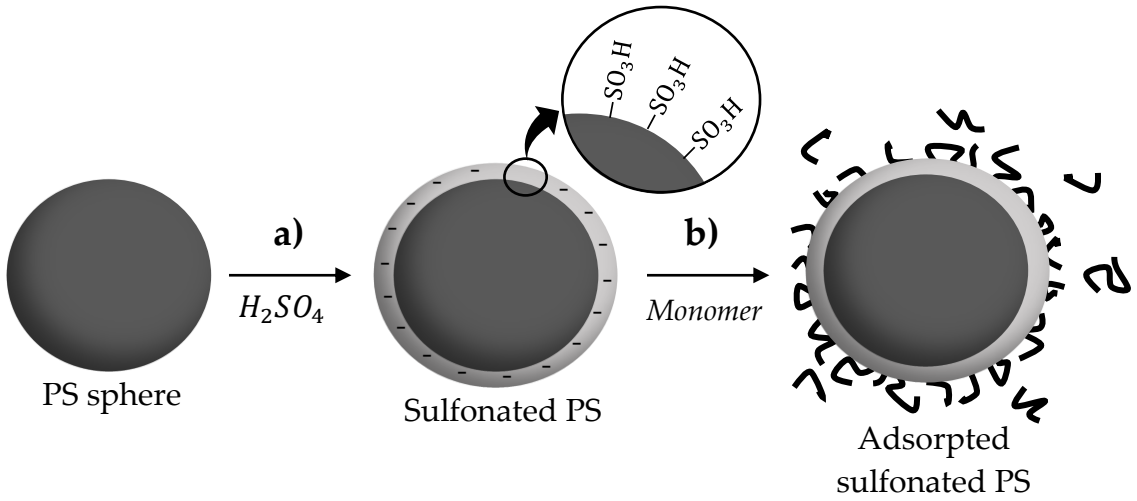

Figure 3.1. Schematic illustration for the fabrication of adsorpted sulfonated polystyrene microspheres. The addition of sulfuric acid results in a **a**) short sulfonation reaction, which removes the tensioactivity of the surfactants; the addition of the monomer leads to its **b**) absorption. This process results in the increase of the surface tension, which promotes their floatation in the air/liquid interface.

3.1.2 Langmuir-Blodgett and dispensing method

Figure 3.2A shows a 2 inches diameter c-Si wafer (250 μm thick) fully covered with a PS colloidal mask previously formed that resulted from a LB process. This highlights the application of these masks over large areas, where the coverable area is only limited by the dimensions of the used equipment, namely the tank and trough.

As presented in Figure 3.2B-C (delimited in red/blue box), the applied wet-coating methodology may lead to defect formation. While dispensing the prepared suspension on the air-liquid interface, the inherent turbulence pushes the spheres against each other, and as the volatile water-immiscible dispersant evaporates an ordered colloidal monolayer is formed. The excessive turbulence may lead to the aggregation of the dispensed spheres into small domains (as in the red box in Figure 3.2B). Though, aggregates are mainly formed due to the direct dispensing method. The implied vertical path of the dispensed spheres causes their immersion and consequent aggregation in the

liquid due to their hydrophobic nature. On the other hand, vacancies (delimited in light blue in Figure 3.2C) are mainly attributable to the low aperture of the compression barriers, resulting in their relatively low packaging and distancing the array from a hexagonal one.[40]

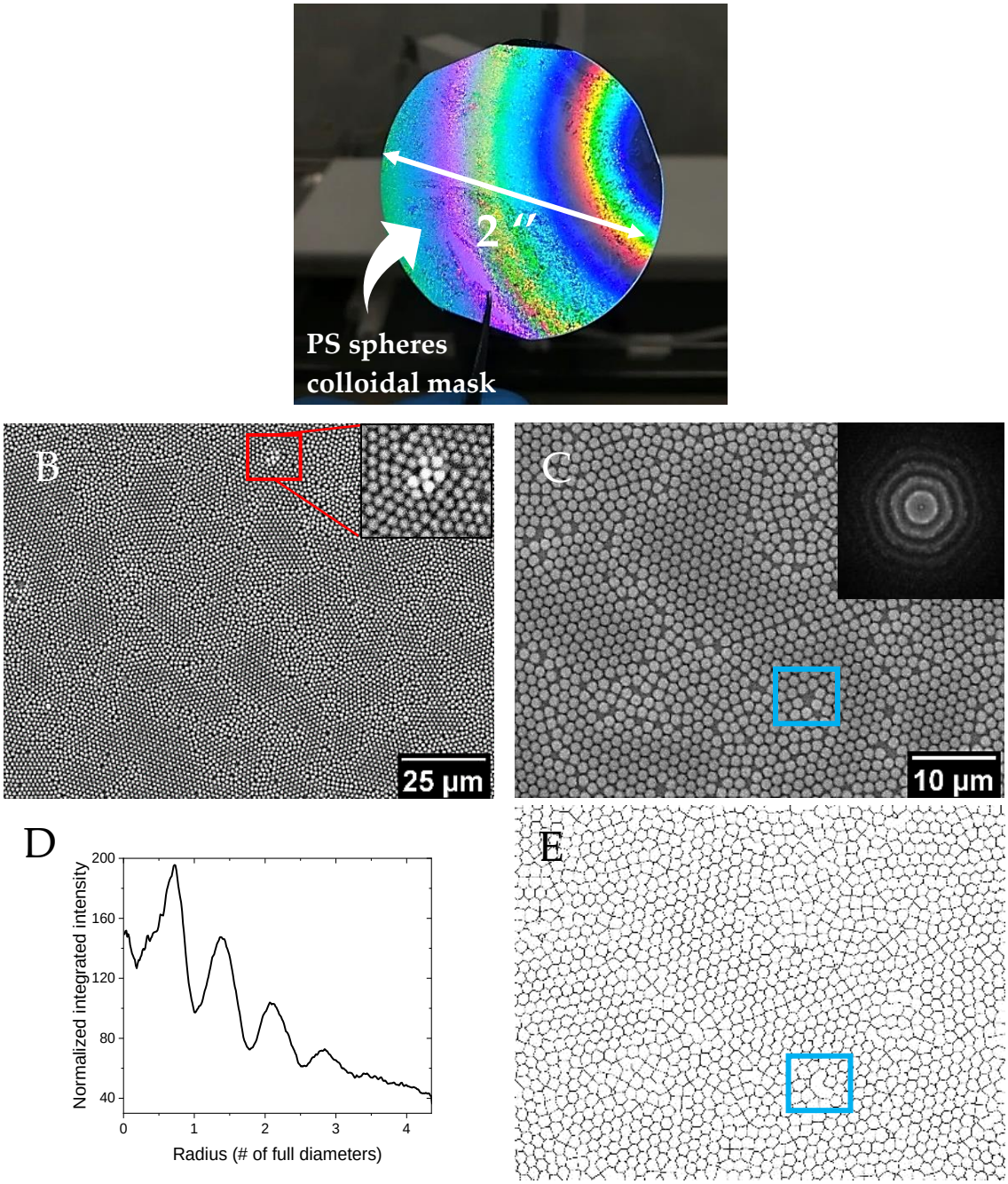

Figure 3.2. (**A**) Digital photograph of a 250 µm conventional flat c-Si wafer (2 inches of diameter) covered with a colloidal mask through LB wet-coating methodology. (**B**) and (**C**) SEM images of the top-view of a PS colloidal mask deposited on a similar conventional c-Si wafer: (**B**) low magnification (1000×) where a spheres aggregate is delimited in a red box (see respective inset). (**C**) higher magnification (3000×) where a vacancy defect is delimited (in light blue box), with corresponding FFT (inset) and (**D**) respective Radial Profile distribution. (**E**) Voronoi diagram of (C) with a vacancy delimited in a light blue box.

A more detailed analysis can be made. The spheres arrangement was assessed by Scanning Electron Microscopy (SEM) images processing, specifically with Fast Fourier Transform (FFT), which evaluates it through the number of distinct rings or the so-called peaks (bright dots). The inset of Figure 3.2C shows four distinct rings with some peaks, which correspond to an intermediate situation between an excellent and poor arrangement. Comparative FFT imagery is presented in Figure SB1 (Appendix B, section 1). This is confirmed with the Radius Profile in Figure 3.2D, determined based on the FFT inset of Figure 3.2C, by presenting four distinct peaks. Thus, a reasonably periodic array was attained due to a good-quality deposition.

The structural homogeneity was appraised by an intuitive approach: the Voronoi diagram. As seen in Figure 3.2E, an almost homogenous honeycomb pattern mainly composed of equilateral hexagons throughout the analyzed area is shown. A PS sphere is usually surrounded by six other identical spheres, as pretended, but also of some vacancies, as exemplified with a light blue box. As a result of this binary representation, this defect is represented with another shape than an hexagonal one. A more detailed description of these image-processing tools is provided in Appendix B section 1.

3.1.3 Dry etching, infiltration, and lift-off

The colloidal mask-shaping process constitutes the next step in the CL methodology. To that end, the deposited PS spheres were submitted to different reactive ion etching (RIE) times, t_{RIE}. Since this first RIE occurs under an O_2 exposure, the PS spheres experience an anisotropic modification of their shape, from spheres to spheroids (see Figure 1.2 in Introduction, CL method 2, steps 1-2), as the etching is mainly directional from the top, following a geometric model already detailed in the literature.[39] Nevertheless, their periodicity and center-to-center distance (pitch) are retained.

The now-created inter-particle space is filled with a high-refractive index material through sputtering. The resultant deposited thickness was determined by simulation (see obtained values in Tables SA4 and SA5, Appendix A, section 3). As the deposited material infiltrates through the free surface areas of the substrate, it continues to grow, surrounding the PS spheres. The infiltrated material first acquires a pyramidal/cone-like shape that continues to grow, and, at some point, the distinct features meet in their base. In this work, it is worth noting that the targeted deposited thickness is typically used to represent the correspondent batch. For further specification the O_2 t_{RIE} or the simulated thickness is also indicated. A second dry etching process is performed with a mixture of

Ar/CF_4, which removes the top capping layer of deposited material, exposing the PS spheroids. Then, the PS spheres are chemically dissolved in toluene assisted by bath sonication for 1 hour. As a result of the spheroids lift-off and second dry etching, the excess deposited thickness will be removed. Hence, thicker structures than the spheroids' minor axis (height) are aimless when applying colloidal lithography methodologies.

3.2 Photonic Nanostructures Characterization

This subsection presents the morphological, optical, and topographical assessment of the voids arrays designed on top of c-Si with different textures and thicknesses: conventional and thin double-side polished c-Si wafers (90 and 250 μm) and etched IBCSCs (140 μm μm c-Si thickness). Preliminary results on textured (130 μm) and flat (740 μm) IBCSCs are presented in Appendix B, respectively, in subsections 2.4 and 2.5. Excluding the latter ones, the electrical performance of all coated solar cells is also assessed. The RIE time and TiO_2 thickness were varied and studied, as they established the optical performance of the final structured coating, i.e., anti-reflection and light scattering effects.[24] The original PS spheres' diameter (~1.3 μm) also impacts these effects but remained constant throughout this work.

3.2.1 c-Si wafers with conventional (250 μm) thickness

3.2.1.1 Morphological assessment

After the colloidal masks deposition through LB, the now-coated c-Si wafers with 250 μm of thickness were submitted to different O_2 t_{RIE}: 100, 200, 300, and 400 seconds. This range embraces smaller ones reported in literature for similar nanostructuring conditions.[7,15,24] These shaped masks were then infiltrated with TiO_2 with three defined targeted thicknesses: 200, 400, and 700 nm (see Table SA4 for simulated thicknesses).

After the lift-off step, these c-Si wafers were covered with the resultant photonic nanostructures, as depicted in the sketch of Figure 3.3A. SEM images of the representative 200 nm TiO_2 batch were taken in random sites of the samples' surface (Figures 3.3B-E). Respective low-magnification top views are exhibited in Appendix B, sub-subsection 2.1.1.

From Figures 3.3B-E, some undesirable PS residues (bright fragments) are shown, suggesting a shorter-than-required applied lift-off time. Nevertheless, the optical performance should not be influenced by these low-size residues in the considered range (350-1400 nm).[8] On the other hand, the increase in the voids interspace is noticeable from

B to E: as the t_{RIE} is increased (see respective insets), the spheres undergo more prolonged exposure to the etching gases, resulting in a continuous size reduction (hence diameter) and shape modification.[39,44] The increase of surface roughness is also observed for longer O_2 t_{RIE}, as reported in literature[45,46] especially for 300-400 s. In this case, not only the t_{RIE} but also the gas (O_2) flow and applied pressure contribute to this effect.[24] Hence, a tune of the gas mixture, flow, and applied pressure is suggested to avoid surface roughening and possibly boost the resulting optical performance for relatively high O_2 t_{RIE} (300-400 s).

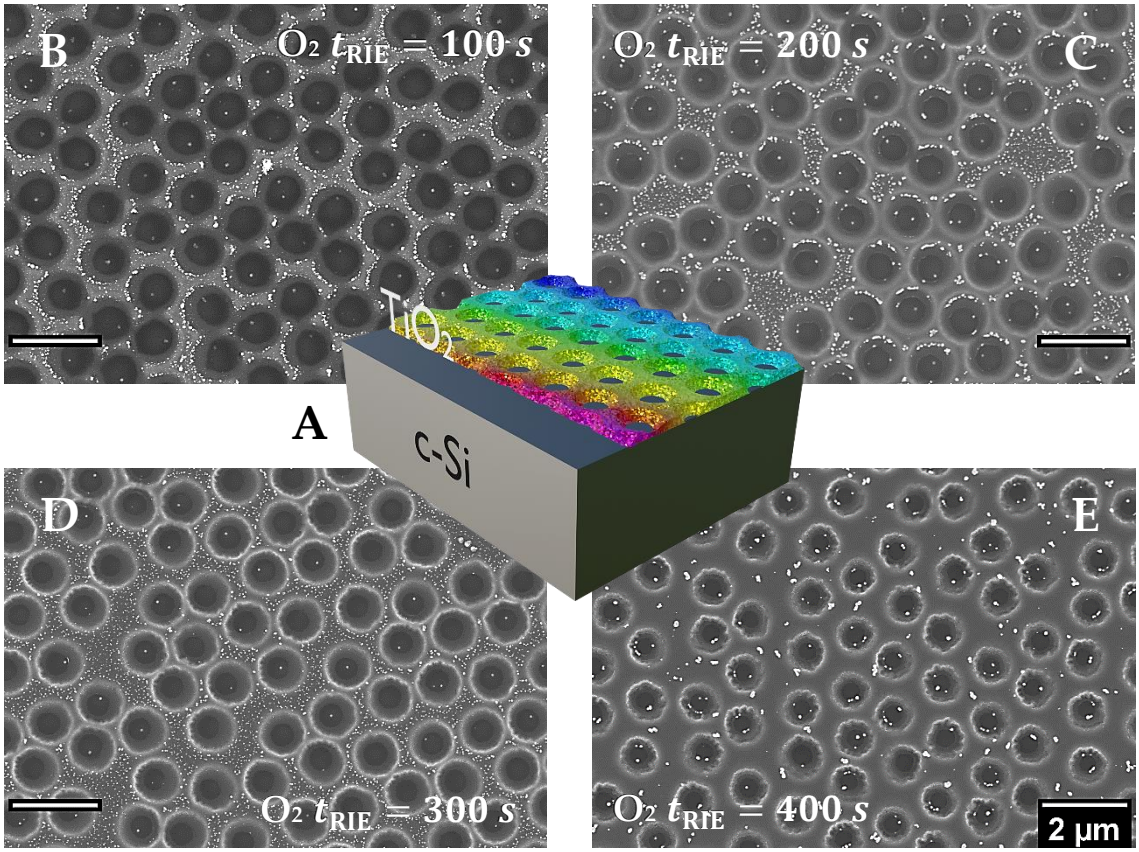

Figure 3.3. (**A**) Sketch of photonic nanostructured voids array on top of thin/thick c-Si wafer. SEM top view imagery of 200 nm of TiO_2 targeted thickness batch (275 ± 15 nm of simulated thickness) photonic nanovoids is shown, resulting from (**B**) 100, (**C**) 200, (**D**) 300 and (**E**) 400 s of O_2 RIE time. The common scale bar is indicated in the bottom right figure (E). See Figure SB2 (Appendix B, sub-subsection 2.1.1) for respective low magnification SEM.

3.2.1.2 Optical assessment

The optical performance of the designed nanostructured coatings on top of conventional c-Si wafers was evaluated from 350-1400 nm via spectrophotometry. Transmittance and reflectance (total and diffuse, full and dashed line, respectively) were measured, and total absorptance was determined as described in the Materials and Methods section.

Figures 3.4A-C comprise the optical measurements of the representative 400 nm TiO_2 targeted thickness batch, which includes the coatings submitted to different O_2 t_{RIE} (100, 200, 300 and 400 s). These are compared to the reference (in black): a flat c-Si wafer (A) without and (B-C) with ~300 nm Ag rear mirror coating.

Before the deposition of the rear mirror, transmittance was assessed. As shown in Figure 3.4A, the employment of the photonic voids array (see the sketch of Figure 3.4A) led to a total transmittance reduction at the longer NIR wavelengths (> 900 nm), when compared to the reference wafer, usually where the majority is diffuse. These are due to their varying cross-sectional shape, which results in their strong forward light scattering. Their consequent confinement within the absorber thus enhances their absorption probability.[10,24] Usually, transmittance in NIR is lower as the O_2 t_{RIE} is higher, except for 300 s (430 nm of TiO_2 simulated thickness), that correspond to the highest transmittance reduction (roughly half).[10,47]

To confine those low-energy photons (> 900 nm), Ag flat rear mirrors were commonly deposited in all samples, as they reflect these photons to the absorber, due to more pronounced refractive index mismatch between the absorber (~4) and the rear mirror (~0.05). As such, reflection and, hence, escape of those photons from the top structured surface is increased (see reflectance spectra of Figures 3.4B and SB3A, Appendix B, sub-subsection 2.1.1). Even though, the internal reflection of those photons gives rise to a more pronounced absorption enhancement, as shown for all samples in Figure 3.4C (for comparison see Figure SB3B, Appendix B, sub-subsection 2.1.1).

In addition to the scattering effect in NIR, the designed coatings also result in a broad light in-coupling effect. As stated previously, a pyramidal-like cross-sectional shape when combined with the high-real part of the TiO_2 refractive index (n~2.5-2.7), provides a geometrical and gradual effective refractive index matching between the air and the absorber, due to presence of the nanocoating in the middle. Subsequently, the abrupt and disruptive relatively low to high n transition (~1 of air and ~4 of silicon) is avoided, inducing a better and broad wave-impedance matching in the sample front and, thus, leading to a wide reflection reduction (UV-VIS-NIR).[10,24] As seen in Figure 3.4B, when compared to the uncoated thick c-Si wafers with rear mirror, the voids array can reduce reflectance nearly up to 50 % in the UV-VIS and 70 % in the NIR range, with the respective parameters combination: 511 and 430 nm TiO_2 (simulated thickness), 400 and 300 s, respectively. On the other hand, several peaks in Figures 3.4B and C are observed in the Visible band. As the O_2 t_{RIE} is greater, the particles interspace is also increased. Hence, the volume of infiltrated material between the resultant spheroids and

TiO_2 planar regions is raised, which causes the intensification of the delocalized constructive/destructive interferences, shown by the observed peaks.

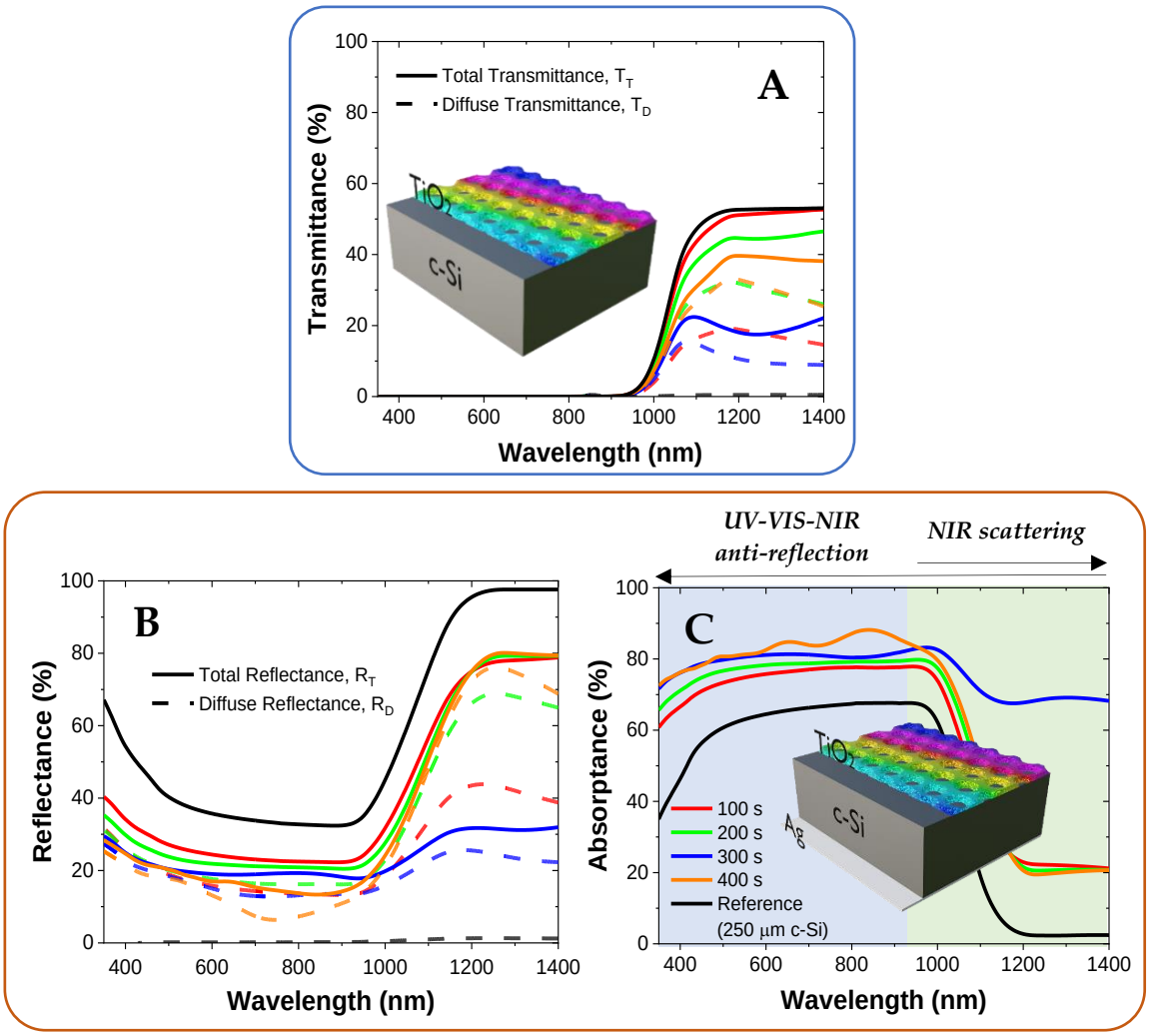

Figure 3.4. Total (full) and diffuse (dash) (**A**) transmittance, (**B**) reflectance and (**C**) calculated total absorptance spectra of the different samples of 400 nm TiO_2 targeted thickness batch for the different O_2 t_{RIE} (100-400 s), compared to the optical performance of original uncoated c-Si wafer (in black). The spectra were measured prior (in a blue box) or after (in an orange box) the Ag rear mirror coating (~300 nm). Simulated thicknesses are the respectively the following: 325 (100 and 200 s), 430 (300 s) and 511 (400 s) nm of TiO_2.

Therefore, as depicted in Figure 3.4C, the anti-reflection and light scattering effects are added. These result in combined light in-coupling and confinement effects, contributing to broad absorption enhancement. Considering all experimental samples with rear mirror, the highest attained absorption depends on the range of interest: (1) in the UV, the highest absorption enhancement was achieved with 511 nm of TiO_2 (O_2 t_{RIE} = 400 s), absorbing ~72 %; (2) in the Visible, the wafer coated with 792 nm of TiO_2 (O_2 t_{RIE} = 300 s) now absorbs up to ~88 %; (3) in NIR, the sample with 430 nm of TiO_2 (O_2 t_{RIE} = 300 s) absorbed up to 70 % due to a more intense light scattering effect.

According to simulation and experimental works,[14,24] high aspect ratio features favor a broad anti-reflection effect in UV-Vis. Then, the highest anti-reflection should be reached with the maximum height, close to the initial PS spheres radius (0.65 μm).[24] However, this is only corroborated in the Visible band, as referred in this paragraph in (2).

The best parameters conjugation that led to the best overall optical performance is not yet clearly distinguished. To that end, the average absorption between 350-1200 nm was computationally determined using the following formula:

$$\langle Abs \rangle_{350-1200} = \frac{\int_{350}^{1200} Abs \, d\lambda}{\Delta\lambda} \quad (1)$$

where the integrated absorptance of each wafer with LT design on top and rear mirror $\left(\int_{350}^{1200} Abs \, d\lambda\right)$ was calculated and divided by the considered wavelength range ($\Delta\lambda$). As shown in the 3D plot of Figure 3.5A, the highest attained average absorption was achieved for 300 s of O_2 $\boldsymbol{t_{RIE}}$ and 430 nm of TiO_2 thickness, reaching ~79 % of average absorption in the mentioned range. Moreover, it is possible to determine the average absorptance enhancement, with respect to the uncoated conventional c-Si wafer with a rear mirror (sketched in the center of Figure 3.5), applying computationally the following expression:

$$E_{<\mathrm{Abs}>}(\,\%) = \frac{\langle Abs \rangle_{\mathrm{LT}} - \langle Abs \rangle_{\mathrm{Reference}}}{\langle Abs \rangle_{\mathrm{Reference}}} \times 100 \quad (2)$$

the average absorptance enhancement $E_{\langle \mathrm{Abs} \rangle}(\,\%)$ of each LT coating is, thus, determined by comparing its average absorption $\langle Abs \rangle_{\mathrm{LT}}$ to the obtained with the reference $\langle Abs \rangle_{\mathrm{Reference}}$, between 350 and 1200 nm. As shown in Figure 3.5B, ~47 % of absorption enhancement is attained with the combination of the abovementioned parameters.

A more in-depth optical analysis can be made. Considering that each absorbed photon generates charged carriers that are then separated and collected in the representative contacts, namely TiO_2 and Ag (thus, internal quantum efficiency of the respective idealized cell equals 100 %), it is possible to determine the resultant photocurrent density (J_{ph}), by integrating the absorption in the absorber layer for the defined range, convoluted with the AM1.5 solar spectrum ($I_{\mathrm{AM1.5}}$ in W m^{-2} m^{-1}):[13]

$$FoM_{\mathrm{op}} = J_{\mathrm{ph}} = e \int_{350}^{1200} \frac{\lambda}{hc} Abs(\lambda) \, I_{\mathrm{AM1.5}}(\lambda) \, d\lambda \quad (3)$$

where e denotes the electrons' elementary charge, λ the Planck's constant, and c the speed of light in vacuum. This formula assumes a perfect scenario, as it neglects any

electrical losses. For this reason, it defines the upper limit of the attainable J_{ph} with a representative solar cell, accordingly. As it is typically used for comparison in literature, it was adopted as optical figure-of-merit (FoM_{op}). As shown in Figure 3.5C, the highest attained J_{ph} was 36.6 mA/cm² for the combination of the following parameters: 792 nm and 300 s of O_2 t_{RIE}. Applying the photocurrent density values instead of average absorption in Equation (2), the photocurrent density enhancements $\left(E_{\mathrm{J}_{ph}}(\%)\right)$ were determined relative to the referred reference and whose resulting values are plotted in Figure 3.5D. A $E_{\mathrm{J_{ph}}}$ of ~37 % for the conditions noted above is noteworthy.

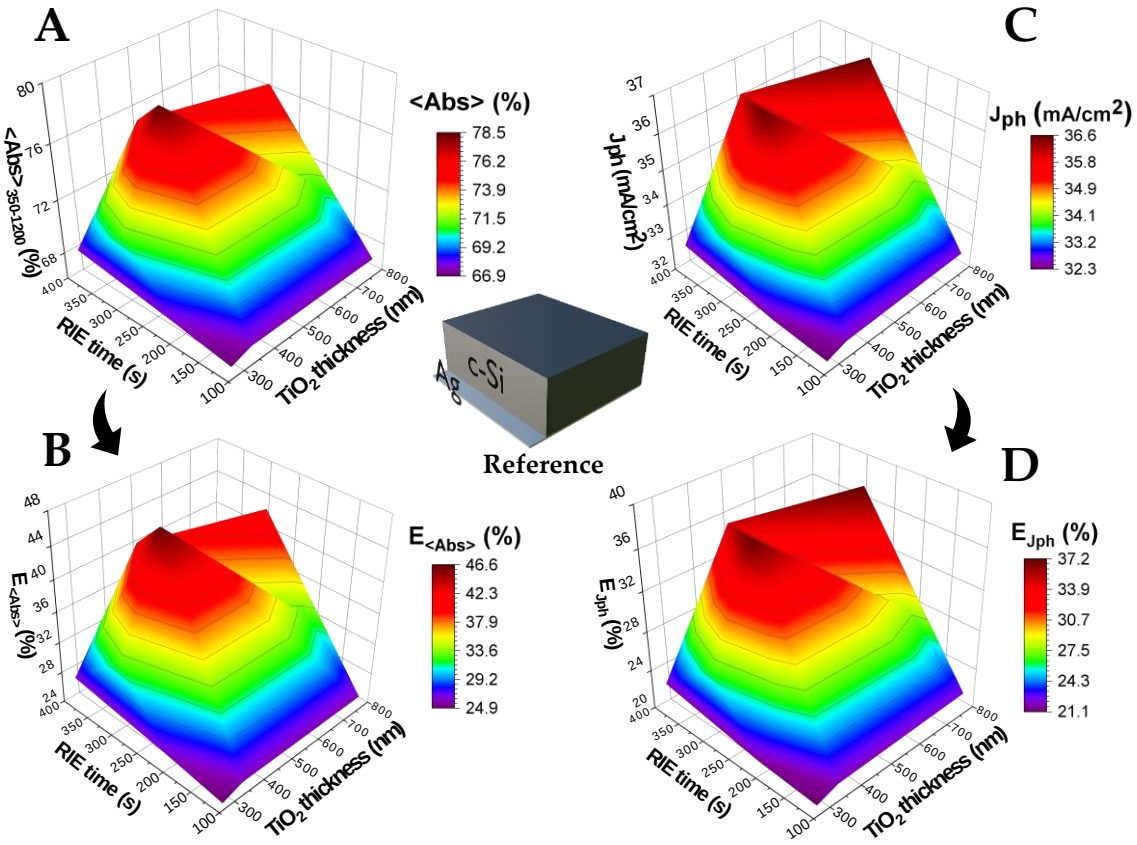

Figure 3.5. 3D plots assessment of (**A**) average absorption $\langle Abs \rangle$ of the selected wavelength (350-1200 nm) and respective (**B**) enhancement $E_{\langle Abs \rangle}$ relative to the considered reference (250 µm thick c-Si wafer with ~300 nm Ag rear mirror, see sketch in the center). (**C**) Photocurrent density (J_{ph}) is also presented and respective (**D**) enhancement $E_{\mathrm{J_{ph}}}$ relative to the same reference for each coated wafer with rear mirror.

Thus far, only the optical enhancement relative to a uncoated c-Si wafer with a rear mirror was evaluated. However, it is common to apply an optimized anti-reflection coating (ARC) on top of the device to minimize reflection at 500-600 nm. As such, a planar TiO_2 film with n~2.6, pre-calculated thickness t and optimized to reduce reflection in 550 nm of wavelength λ $\left(t = \frac{\lambda}{4n} \approx 53\ nm\right)$ was deposited on top of a conventional c-

Si wafer after the deposition of a flat rear mirror (~300 nm Ag). Optically, a strong anti-reflection effect occurs with the applied planar ARC on c-Si (c-Si/pARC, see Figure 3.6A in purple line), between 600-1000 nm but more intense for 600 nm. However, this effect is not as broadly extended as the attained with the best performing nanostructured coating (c-Si/TiO_2 LT orange full line, 792 nm TiO_2, O_2 $t_{RIE} = 300$ s), which is confirmed by the superior $\langle Abs \rangle$ of this latter (see inset of Figure 3.6A). Also, a significant scattering effect in the NIR band is attained with the nanostructures. In this range, the unpatterned coatings do not enhance absorption. Consequently, this LT design led to a higher J_{ph} (36.6 mA/cm²) than the attained with the c-Si/pARC (34.9 mA/cm²), as verified in Figure 3.6B.

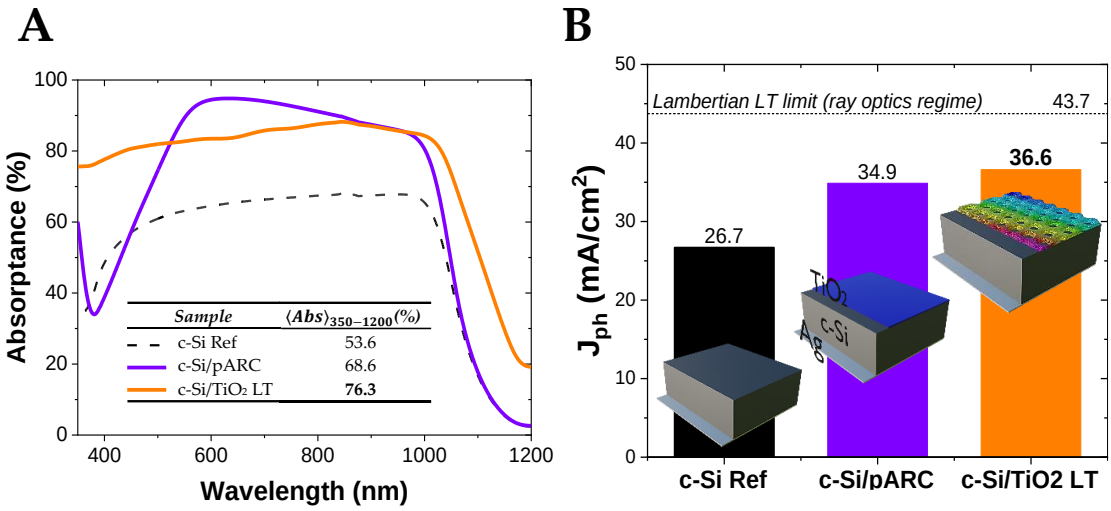

Figure 3.6. (**A**) Absorptance spectrum of flat silicon wafer (reference, c-Si reference), a similar coated wafer with optimized ARC with ~50 nm of TiO_2 (c-Si/pARC) or with LT nanovoids (c-Si/TiO_2 LT, correspondent to 793 nm TiO_2, 300 s of O_2 t_{RIE} sample), in black, purple and orange, respectively. All samples were coated with ~300 nm of flat Ag rear mirror (**B**) Spectrally integrated (350-1200 nm) absorptance, presented regarding J_{ph} for the three samples analyzed in (A) and whose architecture is sketched on top of each bar. The determined J_{ph} of theoretical geometrical optics case of the respective Lambertian limit (~250 µm of c-Si) is marked with horizontal dashed line.

An idealized analytical method can be considered for comparison. Considering light waves as rays and disregarding interference effects, the so-called Lambertian formalism, dependent on the absorber and its thickness, defines the upper bound for absorptance and, hence, J_{ph}. This is considered within the regime of geometrical optics, as it considers not only i) perfect anti-reflection and ii) isotropic scattering at the front but also iii) perfect rear reflector.[24,48,49] Still, the difference between the highest attained value (36.6 mA/cm²) and this conceptual case (43.7 mA/cm²) enables further optical improvements of the here-designed coatings.

3.2.1.3 Topographical assessment

As discussed above, the best-performing (in terms of highest $\langle Abs \rangle$ and J_{ph}) designed features (correspondent to 430 and 792 nm of TiO_2 thickness) result from exposure to O_2 $t_{\mathrm{RIE}} = 300$ seconds. To determine the features' dimensions behind such significant optical performance, the topography of the samples' surface was determined via Atomic Force Microscopy (AFM), which is shown below in Figure 3.7.

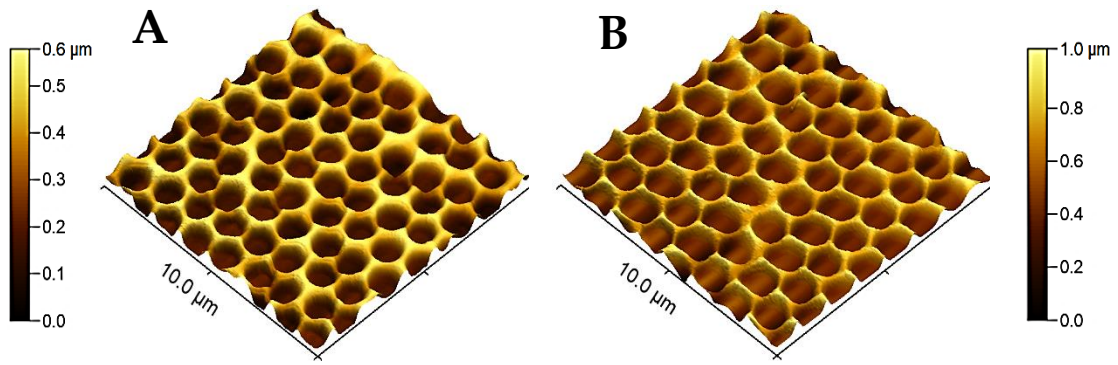

Figure 3.7. 3D orthographic projection of AFM of 10 × 10 µm² top-views (see Figures SB4 A1-B1, Appendix B, sub-subsection 2.1.2) of the two nanostructured coatings on conventional (250 µm) c-Si wafer respectively with the highest $\langle Abs \rangle$ and J_{ph}: (**A**) targeted thickness of 0.400 µm TiO_2, with determined average height of TiO_2 0.429 ± 0.070 µm and equivalent (simulated) film thickness of 0.430 µm; (**B**) targeted thickness of 0.600 µm TiO_2, with obtained average height of TiO_2 0.669 ± 0.055 µm and equivalent film thickness of 0.792 µm. Both are resultant of 300 seconds of RIE (O_2) time. Respective height scales bars are presented.

The curved nature of the designed features and their ordered arrangement are visible above. Additionally, it was possible to correlate the structures' average height (see Figure SB4, Appendix B, sub-subsection 2.1.2) with the equivalent (simulated) TiO_2 film thickness. As expected, the equivalent film thickness is even slightly higher than the designed features' average height. That is owing to the fact that the average height accounts for the small portion of TiO_2 removed by exposure to Ar/CF_4 gases mixture since the AFM measurements were performed after that exposure, contrary to the simulations. Additionally, besides the PS spheres diameter (~1.3 µm), which defines the array pitch, and the $t_{\mathrm{RIE}} = 300$ s, which defines the mesh line width, the dimension of the remaining feature - average height - that induce a higher $\langle Abs \rangle$ or J_{ph} are respectively the following: (A) 0.429 ± 0.070 and (B) 0.669 ± 0.055 µm. It is worth noting that further simulations account for the TiO_2 remotion resultant of the second dry etching process.

3.2.2 *c-Si wafers with thin (90 μm) thickness*

The discussion in the previous sub-subsection can be transposed to thinner (90 μm) flat c-Si wafers. In this case, the TiO_2 target thicknesses were the following: 450, 500, and 700 nm. The O_2 t_{RIE} took the following values: 250, 300, and 350 seconds. Therefore, it was possible to replicate the parameters that resulted in higher $\langle Abs \rangle$ or J_{ph} attained with the conventional c-Si wafers and to evaluate the resultant optical performance in a wide range of parameters. This sub-subsection constitutes an optical comparison to the thicker (250 μm) wafers. As such, only the optical performance of these will be addressed.

When applied in the 90 μm wafers, a significant broad absorption enhancement is obtained, concerning the original flat c-Si wafers, as seen in Figure 3.8A, similarly to the conventional (250 μm) wafers. This results from the combination of light scattering in longer wavelengths (> 900 nm) and broad anti-reflection effects, as respectively seen in the transmittance and reflectance spectra of Figures SB5A-B (Appendix B, subsection 2.2), respectively.

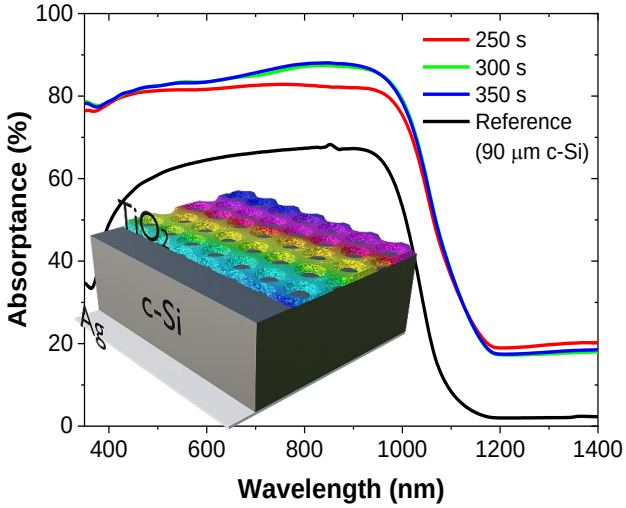

Figure 3.8. Absorptance spectrum relative to 90 μm flat c-Si wafers coated with photonic nanostructures with 693 nm of TiO_2 simulated thickness, for the various O_2 t_{RIE}: 250, 300 and 350 seconds. All samples were coated with ~130 nm of Ag rear mirror.

Moreover, a more direct comparison can be made by evaluating the respective $E_{\langle Abs \rangle}$ and $E_{J_{ph}}$ determined as described in the previous sub-subsection. As seen in Figure 3.9A-B, both enhancements are more significant as the TiO_2 thickness and RIE time (O_2) are both higher, reaching more than 45 % of $E_{\langle Abs \rangle}$ and 39 % of $E_{J_{ph}}$ with 693 nm of TiO_2 (simulated thickness) and 300 or 350 seconds of O_2 t_{RIE}. However, it is worth noting that the optimal parameters were not yet found for these thin wafers, as clearly seen in the

3D plots. Still, as a result of the tested parameters, both higher $E_{\langle \mathrm{Abs} \rangle}$ and $E_{\mathrm{J_{ph}}}$ are attained, regarding the conventional ones that reached ~42 and 37 %, correspondingly. According to literature, the application of these photonic nanostructured coatings, as of other LT approaches, is more beneficial for thinner absorber films, although the lower the maximum $\langle Abs \rangle$ and J_{ph}, as shown with the attained values presented in Table 1.[10] Hence, even higher $E_{\langle \mathrm{Abs} \rangle}$ and $E_{\mathrm{J_{ph}}}$ are expected for a wider window of tested parameters (higher O_2 t_{RIE} and TiO_2 thickness).

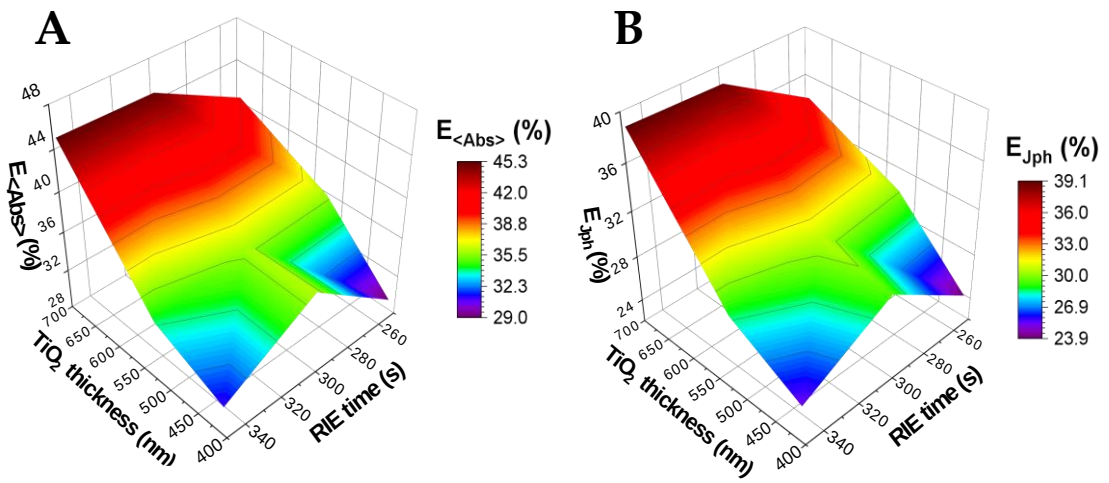

Figure 3.9. 3D plots of (A) average absorption enhancement of all 90 µm wafers experimentally designed with nanostructured coating for the selected wavelength (350-1200 nm), determined relative to the considered uncoated wafer, for the different O_2 t_{RIE} and TiO_2 thicknesses. All samples were coated with ~130 Ag rear mirrors. (B) Respective photocurrent density enhancement, determined regarding the same reference.

Figure SB6 (Appendix B, subsection 2.2) shows the optical performance of the best-performing sample (both in terms of the $E_{\langle \mathrm{Abs} \rangle}$ and $E_{\mathrm{J_{ph}}}$) compared to the one of the uncoated (c-Si Ref) and of a ~50 nm TiO_2 optimized planar ARC (c-Si/pARC) wafers, all coated with a rear mirror. The best-performing wafer coated with photonic nanostructures (693 nm of TiO_2 and 350 s, c-Si/TiO_2 LT) attained a higher broadband absorption (~74 %) when compared to both c-Si Ref (~51 %) and c-Si/pARC (~65 %), as a result of from the combination of the intense light scattering and broad anti-reflection effects, as discussed for the conventional wafers.

The determined J_{ph} for the photonic nanostructured coatings are still far from the Lambertian LT limit (see Table 1), which entails further improvements. Reported simulation and experimental works present a closer J_{ph} to the Lambertian LT limit, determined for flat c-Si wafer thicknesses between 20 and 190 µm, reaching up to 99.8 % of the theoretical (Lambertian) ones, using nanotexturing processes on front and rear

surfaces, that assure broadband anti-reflection and light scattering effects, respectively.[16,50] These compete with the 83,8 % attained with the photonic nanostructured coatings on the conventional and thin (250 and 90 μm, respectively) wafers presented in this work. However, as described in the Introduction, texturing processes hamper the electrical performance of solar cells via recombination losses. As such, despite the poorer absorption enhancements regarding the latest state-of-the-art (to the authors' knowledge), both electrical and optical performances (hence enhancements) of these nanostructures on interdigitated back contact c-Si solar cells are discussed in the following sub-subsection.

Table 1. Maximum $\langle Abs \rangle_{\mathrm{LT}}$ and J_{ph} values (350-1200 nm) attained with front photonic nanostructured coatings applied on top of conventional and thin flat c-Si wafers (250 and 90 μm thickness, respectively) under the respective experimental conditions (respectively TiO_2 simulated thickness and O_2 t_{RIE}): 792 nm, 300 s, and 693 nm and 350 s. The $E_{\langle Abs \rangle}$ were determined relative to the respective not-coated wafers. The J_{ph} values of respective optimized planar anti-reflection coating with ~50 nm TiO_2 in the front surface are also indicated. The J_{ph} enhancements attained with the wave-optical LT structures were determined concerning the uncoated wafers $\left(E_{\mathrm{J_{ph}}}\right)$ and to the ARC $\left(E_{\mathrm{J_{ph}}}^{\mathrm{ARC}}\right)$. All samples were coated with ~300 nm Ag of rear mirror. The applied coatings are also compared with Lambertian scattering surfaces in terms of J_{ph} determined for the referred samples for the indicated wafer thicknesses. $J_{\mathrm{ph}}^{\mathrm{Lamb.}}$ correspond to the respective calculated percentages concerning the Lambertian LT limit (100 %).

	Wave-optical LT structure						**Lambertian LT limit**	
Wafer thickness (μm)	$\langle \mathbf{Abs} \rangle_{\mathbf{LT}}$	$\mathbf{E}_{\langle \mathbf{Abs} \rangle}$	$\mathbf{J_{ph}}$ **(mA/cm²)**	$\mathbf{E}_{\mathbf{J_{ph}}}$	$\mathbf{J_{ph}^{ARC}}$ **(mA/cm²)**	$\mathbf{E}_{\mathbf{J_{ph}}}^{\mathbf{ARC}}$	$\mathbf{J_{ph}^{Lamb}}$ **(mA/cm²)**	$\frac{\mathbf{J_{ph}}}{\mathbf{J_{ph}^{Lamb.}}}$
250	76 %	42 %	36.6	37 %	34.9	5 %	43.7	84 %
90	74 %	45 %	35.6	39 %	33.2	7 %	42.5	

LT, Light trapping; *ARC*, Anti-reflection coating; *Lamb*, Lambertian.

3.2.1 Photonic coatings on etched IBCSCs

Figure 3.10 shows the tilted view (45°) photonic nanostructured coating composed of TiO_2 on top of the originally etched IBCSC with 140 μm of c-Si absorber. Although the pristine solar cells present a microscale roughness (see Figure SB7, Appendix B subsection 2.3), the designed nano-features are still well-defined on top of them, due to their considerably lower wavelength-range dimensions. Despite the few defects (as vacancies, e.g.), the discussed CL methodology results in a short and long-range ordered voids array, which covers the etched surface homogeneously. In this case, the O_2 t_{RIE}

was maintained (300 seconds), while the TiO_2 thickness was varied, resulting in the following simulated thickness: 281, 423, 448, 545, and 885 nm. The resulting optical and electrical performances are then compared to a uncoated etched IBCSC (eIBCSC).

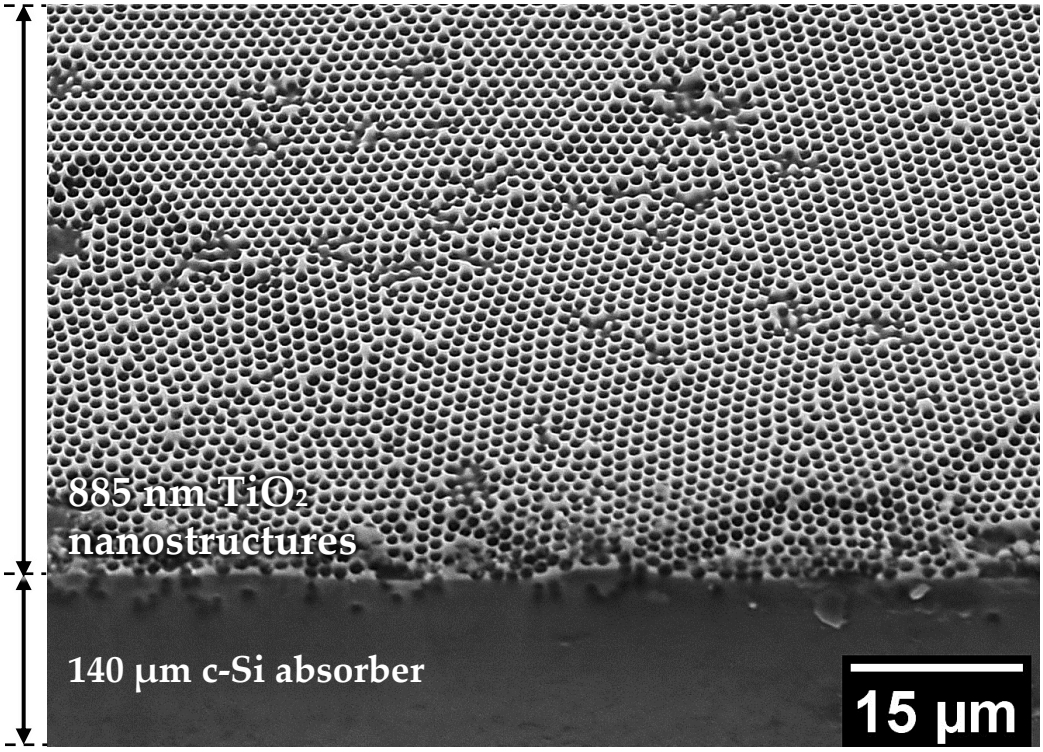

Figure 3.10. SEM tilted-view (45°) of etched IBCSCs (140 μm of c-Si absorber) endowed with photonic nanostructured coatings (885 nm TiO_2, O_2 $t_{RIE} = 350$ s).

Similarly to the conventional and thin c-Si wafers, the application of these photonic coatings results in the following combined effects: light scattering of longer-wavelength photons (> 900 nm) and broad anti-reflection effects (see Figure SB8 Appendix B, subsection 2.3, namely transmittance and reflectance spectra). These result in a broad absorption enhancement along the wavelength range of study (350-1200 nm), which includes the "useful" absorption of c-Si (< 1200 nm). The thickest coating (885 nm TiO_2) reached ~77 % of $\langle Abs \rangle$ in the selected range (see inset of Figure 3.11A), where the respective reference (uncoated eIBCSC, in black) only achieved ~52 %. These values were determined using Equation 1 (sub-subsection 3.2.1). Therefore, both short-circuit current density (J_{sc}) and, hence, efficiency enhancements are expected to be attained with all samples, these being maximum with the thickest coating (885 nm of TiO_2 infiltration thickness), not only due to the highest $\langle Abs \rangle$, when compared to thinner coatings, but also to the fact that the attained absorption is the greatest for all wavelengths.

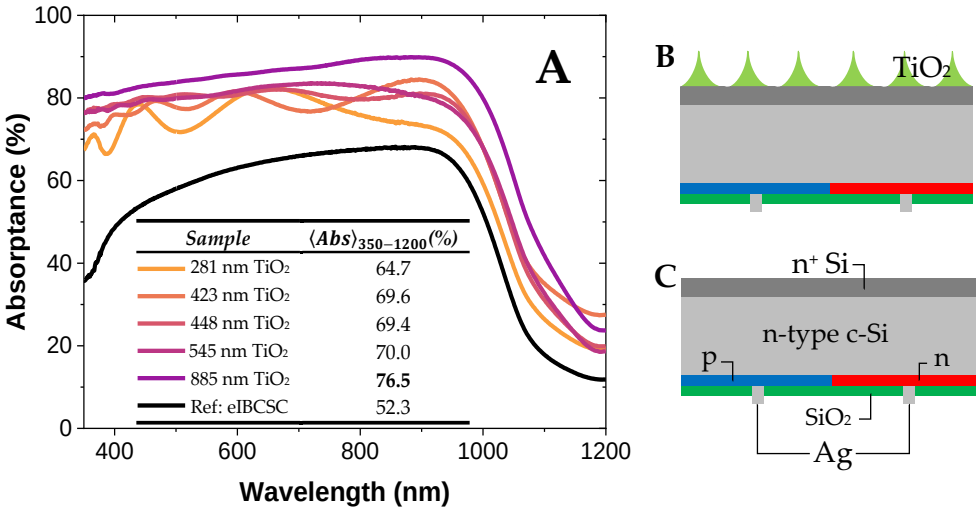

Figure 3.11. (**A**) Absorptance spectrum of etched IBCSCs (eIBCSCs) with photonic nanostructures (see sketched in **B**) for the common t_{RIE} = 300 s and different TiO_2 thicknesses (simulated): 281, 423, 448, 545 and 885 nm. These are compared to the etched IBCSC reference (in black). Typical IBCSC architecture is sketched in (**C**). Respective average absorption determined between 350 and 1200 nm are presented in inset of (**A**).

We note that it was not possible to electrically measure all the available test cells, as the printed contacts of the remaining samples were severely damaged due to the high temperature inherent to the respective long TiO_2 sputtering times. The presented ones, (≥ 448 nm TiO_2) were submitted to shorter interspersed sputtering processes to preserve their electrical performance. Nevertheless, the optical gains provided by the applied coatings result in substantial electrical performance improvements, as seen in Figure 3.12. The correspondent J-V curves are presented in Figure 3.12A, regarding uncoated an eIBCSC as reference (black dashed lines). In turn, Figure 3.12B-C show the external quantum efficiency (EQE) curves (and respective enhancement) for TiO_2 thicknesses ≥ 545 nm. The absorptance enhancements referred above translate in terms of (1) J_{sc} enhancement (see Figure 3.12A) and (2) broadband EQE enhancement in the considered range (350-1200 nm), but only for TiO_2 thicknesses ≥ 545 nm. This is more perceptible for longer wavelengths (> 900 nm) as a result of the combination of both effects offered by these coatings (anti-reflection and light scattering), reaching more than 150 % of EQE enhancements with the highest features (885 nm of TiO_2).

Therefore, for normal incident illumination, these result in a **pronounced power conversion efficiency** (PCE) **improvement (up to 30 %) that even surpasses the J_{sc} gains (up to 27 %)** for thicknesses ≥ 545 nm of TiO_2, as seen in Figure 3.12E in grey and black lines, respectively. In red edges (in Figures 3.12D-E), maximum PCE and J_{sc} improvements are attained with the thickest coating (**885 nm TiO_2, O_2 t_{RIE} = 300 s**). Still

regarding the latter, enhancements are not equivalent due to the slight electrical enhancement of the open-circuit voltage.

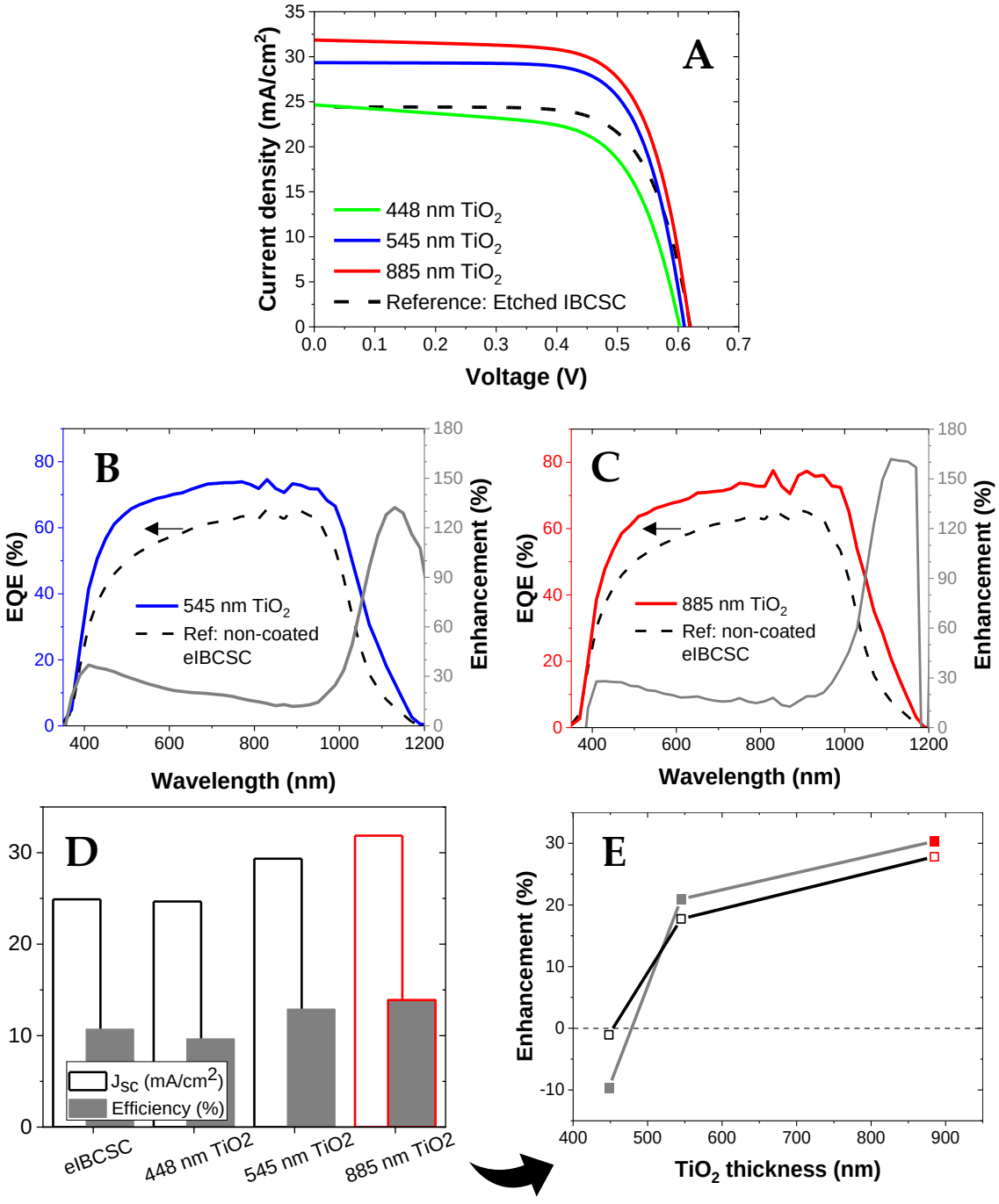

Figure 3.12. (**A**) J-V curves and external quantum efficiency obtained for the eIBCSC coated with photonic nanostructured coatings with (**B**) 545 nm (in blue) and (**C**) 885 nm TiO_2 (in red). In green, only the J-V curve for the eIBCSC covered with 448 nm TiO_2 thickness of nanostructured coating. In every case, the solid lines correspond to the coated solar cells, whose enhancements (in grey lines) are determined with respect to the uncoated etched IBCSC (Reference, in black dashed lines). (**D**) Measured efficiency and short-circuit current density (J_{sc}) values for the IBCSCs coated with the photonic nanostructures with 448, 545 and 885 nm of TiO_2. (**E**) Respective enhancement values with respect to the uncoated etched IBCSC reference.

For the first time, this shows that these LT coatings, composed of wavelength-sized features, result in substantial optical and electrical gains, even when applied directly on thick absorbers.

3.2.1.1 Angular performance

For practical photovoltaic applications, it is crucial to evaluate the electrical response of these solar cells under oblique incidence, given operation without sun-tracking mechanisms.

The electrical performance of the engineered cells was measured under sunlight incidence for the following oblique incidence interval: 0-90°, with a 10° step. The summarized results are presented in Figure 3.13 for the eIBCSCs coated with photonic nanostructures with 545 and 885 nm of TiO_2. The respective evolution of the J-V curves is shown in Figure 3.13A for both samples. As a result of reflection losses with the increase in the light incidence angle (LIA), the power output is diminished. As such, it is shown the overall decrease in generated current and voltage with the increase of LIA, which are maximum for 0° (light incidence normal to solar cells, SCs, top surface) and minimum for 90° (light incidence parallel to top surface).

The dependence on the open-circuit voltage (V_{oc}), J_{sc}, fill factor (FF), and PCE) with LIA is more accurately shown in Figure 3.13B. Enhancements regarding PCE and J_{sc} are shown in Figure 3.13C, determined concerning the uncoated eIBCSC (reference). Although the angular response attained with the photonic nanostructures seems unaffected by the incidence angle increase, shown by the similar trends between the coated (solid lobes) and uncoated etched cells (dashed lobes), the application of these coatings led to superior J_{sc} (hence also efficiency), as indicated in Figure 3.13C. For normal incidence LIA, the highest attained PCE is ~14 % with the solar cells with the thicker coating (885 nm TiO_2), resulting in an unprecedented ~30 % respective gain.

Furthermore, it is seen that these LT coatings are even more beneficial for oblique illumination. Both PCE and J_{sc} present a similar growth with the increase of LIA, up to 80°: with 545 nm of TiO_2, it reaches up to 63 % and 58 %, as with 885 nm of TiO_2, it achieves 33 % and 68 %, respectively. This is due to the outstanding angular acceptance of sunlight waves provided by the curved nanostructured voids,[10,13,14] contrastingly to the uncoated eIBCSCs. Hence, particularly evident for the 545 and 885 nm TiO_2 coatings, remarkable absorption (thus photocurrent and efficiency also) enhancement attained with these LT photonic nanostructured coatings is here shown for the first time, as entailed.

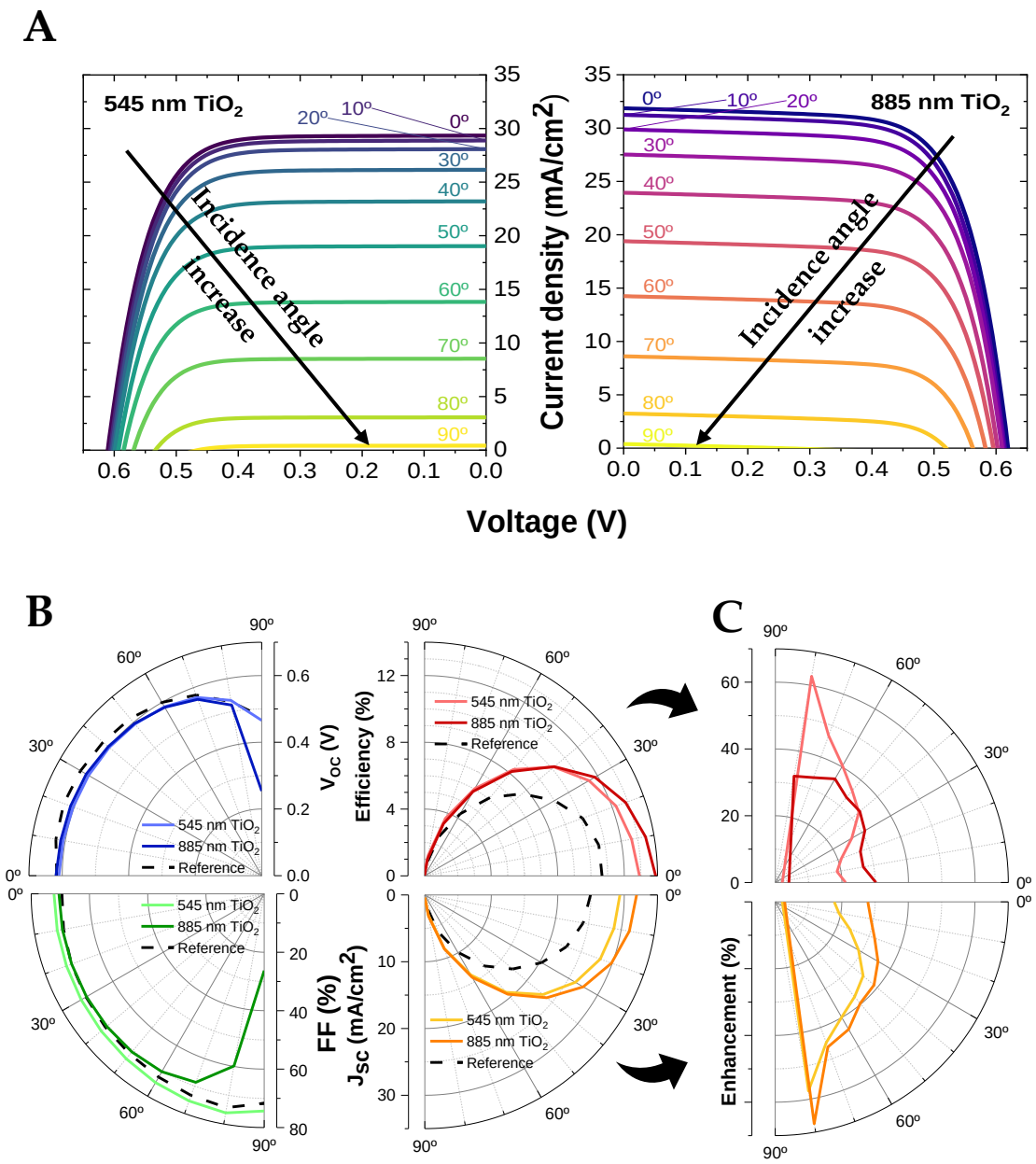

Figure 3.13. (**A**) J-V curves of the eIBCSCs covered with top photonic nanostructured coatings with 545 (left) and 885 nm TiO_2 (right), showing mainly the evolution with the incidence angle, from 0° (light incidence normal to SC top surface) and 90° (parallel to top surface), with a 10° step. (**B**) Polar plots with respect to angular response in terms of (V_{oc} in blue, FF in green, PCE in red and J_{sc} in orange). Solid lines correspond to the LT coating, where lighter colors are respective to 545 nm TiO_2, hence darker to 885 nm TiO_2 nanostructured coatings. Dashed lines correspond to the original uncoated eIBCSC as reference (black dashed lines). (**C**) Enhancements regarding PCE (top) and J_{sc} (bottom), determined with respect to the considered uncoated etched IBCSC reference.

4

CONCLUSIONS AND FUTURE PERSPECTIVES

A successful colloidal lithography (CL) methodology is presented as a flexible gateway to light management in thick crystalline silicon (c-Si) absorbers, as typically presented in the literature for thin or ultrathin films. Hence, through the application of the here-designed photonic nanostructured coatings, an effective broadband light trapping (thus absorption enhancement) is presented for conventional and thin flat c-Si wafers and etched interdigitated back contact solar cells (IBCSCs) as a last-processing step.

Despite the exceptional optical enhancements attained, several considerations regarding the CL method must be deemed. The applied CL methodology resulted in a low defect density of the formed array. These defects, namely aggregates and vacancies, were mainly caused by the direct (vertical) dispensing method and the low aperture of the compression barriers, respectively. To overcome the first one, research suggests an **angled dispensing method** through the simple usage of a 45° tilted glass (see ref.[36] for more details). In turn, regarding the second one, the same literature suggests the **control of surface pressure**, contrasting with the visual inspection performed in this work. Then, it is possible to initiate the Langmuir-Blodgett process just before reaching the point when the array ruptures (called collapsing point), assuring the optimum barriers aperture and the colloidal mask short and long-distance order. Furthermore, it is possible to avoid severe roughening of the PS spheres (caused by the O_2 etching step, as observed for 400 s of O_2 reactive ion etching time, t_{RIE}), exposing them to a **less aggressive etching** and introducing argon into the plasma chamber.[39,45] With this, a long size reduction and shape modification should be achievable while avoiding surface roughening.

Thin and conventional c-Si wafers with respectively 90 and 250 μm thickness were endowed with photonic nanostructured coatings, varying the titanium dioxide (TiO_2) thickness and t_{RIE}. The designed arrays resulted in a broad anti-reflection effect, which was usually greater with high aspect ratio features, respectively designed with thicker coatings, as it comes close (or surpassed) to the initial PS spheres radius.[24] However, typically, these also led to a more intense light scattering effect, which does not follow the previous simulation works on thin-films.[14] Hence, further simulation works should be projected to address this issue.

Regarding the conventional (250 μm) wafers, the attained average absorption $\langle Abs \rangle$ was maximum for 429 nm of TiO_2 and 300 s of O_2 t_{RIE}: up to 79 %, between 350-

1200 nm. This translates into ~47 % of average absorption gain for the uncoated wafer with a rear mirror. However, with 669 nm of TiO_2 and O_2 $t_{RIE} = 300$ s, the integrated absorptance spectrum in the same range convoluted with the solar photon flux resulted in the maximum implied photocurrent density (J_{ph}) of 36.6 mA/cm². Likewise, but with respect to the thinner wafers, the following values were similarly achieved with 693 nm of TiO_2 and 350 of O_2 t_{RIE}: 74 % of $\langle Abs \rangle$, hence ~45 % of gain relative to the uncoated wafer with rear mirror; 35.6 mA/cm² of calculated J_{ph}, thus a gain of ~39 %. Greater $\langle Abs \rangle$ and J_{ph} enhancements are expected for the 90 μm wafers, with further studies that engage a wider window of tested parameters (higher O_2 t_{RIE} and TiO_2 thickness). The above-referred samples show 5 and 7 % of J_{ph} gain, relative to optimized planar ARCs, respectively with 250 and 90 μm c-Si wafers. Nevertheless, a 99.8 % maximum theoretical J_{ph} (Lambertian LT limit) calculated for the same wavelength range and thinner wafers (< 35 μm) are reported for c-Si textured substrates, being the closest experimental evidence of the $4n^2$ classical absorption limit. These compete with the maximum **83.8 %** achieved with the here-coated c-Si wafers. Further CL-fabrication parameters optimization should outline less pronounced reflection losses.

The application of these coatings on textured IBCSCs resulted in a considerable diminishment both in terms of optical and electrical performances and in promising preliminary optical results regarding thick (740 μm c-Si) flat IBCSCs (see respectively Appendix B, subsection 2.4 and 2.5). When applied on thick (140 μm) etched IBCSCs, significant improvements were realized. In this case, the shown broadband absorption enhancement was maximum for the thickest nanostructures (885 nm TiO_2) due to a greater broad anti-reflection and light scattering (900-1200 nm) effects, rendered by those highest aspect ratio features. Without diminishing the original electrical performance, outstanding short-circuit current density (J_{sc}, hence power conversion efficiency, PCE) gains were attained for TiO_2 thicknesses ≥ 545 nm. For normal light incidence angle (LIA), a PCE of 13.9 % and J_{sc} of 31.9 mA/cm² (respective ~30 and ~28 % of gains) were reached with the thickest coating (885 nm). This is still far from the highest attained reported in literature with a standard textured IBCSC with similar architecture and c-Si thickness (25.2 % of PCE[52]). Unmatched angular acceptance enhancements were showed in terms of PCE and J_{sc} at 80° of LIA, with 545 nm of TiO_2 (63 and 58 %, respectively) and with 885 nm of TiO_2 (33 and 68 %, correspondingly). Future works should aim for optical and, hence, electrical performance enhancements, optimizing the applied CL method with the suggestions referred above. Still and subsequently, a highly promising path for c-Si photovoltaic improvements with straightforward near-future integration in the established industry is here projected.

References

1. Schmela M. *SolarPower Europe (2022): Global Market Outlook for Solar Power 2022-2026*; **2022**.
2. Oliveira RD, Mouquinho A, Centeno P, et al. Colloidal lithography for photovoltaics: An attractive route for light management. *Nanomaterials*. **2021**; https://doi.org/10.3390/nano11071665.
3. Breyer C, Bogdanov D, Aghahosseini A, et al. Solar photovoltaics demand for the global energy transition in the power sector. *Prog Photovoltaics Res Appl*. **2018**; https://doi.org/10.1002/pip.2950.
4. Kannan N, Vakeesan D. Solar energy for future world: - A review. *Renew Sustain Energy Rev*. **2016**; https://doi.org/10.1016/j.rser.2016.05.022.
5. Tawalbeh M, Al-Othman A, Kafiah F, Abdelsalam E, Almomani F, Alkasrawi M. Environmental impacts of solar photovoltaic systems: A critical review of recent progress and future outlook. *Sci Total Environ*. **2021**; https://doi.org/10.1016/j.scitotenv.2020.143528.
6. Green MA. Commercial progress and challenges for photovoltaics. *Nat Energy*. **2016**; https://doi.org/10.1038/nenergy.2015.15.
7. Sanchez-Sobrado O, Mendes MJ, Haque S, et al. Lightwave trapping in thin film solar cells with improved photonic-structured front contacts. *J Mater Chem C*. **2019**; https://doi.org/10.1039/c8tc06092d.
8. Boane JLN, Centeno P, Mouquinho A, et al. Soft-Microstructured Transparent Electrodes for Photonic-Enhanced Flexible Solar Cells. *Micro*. **2021**; https://doi.org/10.3390/micro1020016.
9. Efaz ET, Rhaman MM, Imam S Al, et al. A review of primary technologies of thin-film solar cells. *Eng Res Express*. **2021**; https://doi.org/10.1088/2631-8695/ac2353.
10. Mendes MJ, Sanchez-Sobrado O, Haque S, et al. *Wave-Optical Front Structures on Silicon and Perovskite Thin-Film Solar Cells*.; **2019**. https://doi.org/10.1016/B978-0-08-102762-2.00009-4.
11. Lee TD, Ebong AU. A review of thin film solar cell technologies and challenges. *Renew Sustain Energy Rev*. **2017**; https://doi.org/10.1016/j.rser.2016.12.028.
12. Ginley D, Renewable N. Solar Energy Conversion Toward 1 Terawatt. *MRS Bull*. **2008**; https://doi.org/10.1557/mrs2008.71.
13. Haque S, Alexandre M, Mendes MJ, Águas H, Fortunato E, Martins R. Design of wave-optical structured substrates for ultra-thin perovskite solar cells. *Appl Mater Today*. **2020**;. https://doi.org/10.1016/j.apmt.2020.100720.
14. Mendes MJ, Araújo A, Vicente A, et al. Design of optimized wave-optical spheroidal nanostructures for photonic-enhanced solar cells. *Nano Energy*. **2016**; https://doi.org/10.1016/j.nanoen.2016.05.038.
15. Sanchez-Sobrado O, Mendes MJ, Mateus T, et al. Photonic-structured TCO front contacts yielding optical and electrically enhanced thin-film solar cells. *Sol Energy*. **2020**; https://doi.org/10.1016/j.solener.2019.11.051.
16. Ingenito A, Isabella O, Zeman M. Experimental Demonstration of 4n2 Classical Absorption Limit in Nanotextured Ultrathin Solar Cells with Dielectric Omnidirectional Back Reflector. *ACS Photonics*. **2014**; https://doi.org/10.1021/ph4001586.

17. Vicente A, Águas H, Mateus T, et al. Solar cells for self-sustainable intelligent packaging. *J Mater Chem A*. **2015**; https://doi.org/10.1039/c5ta01752a.

18. Águas H, Mateus T, Vicente A, et al. Thin Film Silicon Photovoltaic Cells on Paper for Flexible Indoor Applications. *Adv Funct Mater*. **2015**; https://doi.org/10.1002/adfm.201500636.

19. Vicente AT, Araújo A, Mendes MJ, et al. Multifunctional cellulose-paper for light harvesting and smart sensing applications. *J Mater Chem C*. **2018**; https://doi.org/10.1039/c7tc05271e.

20. Manuel J, Fortunato E, Martins R, et al. Optimal-Enhanced Solar Cell Ultra-thinning with Broadband Nanophotonic Light Capture Optimal-Enhanced Solar Cell Ultra-thinning with Broadband Nanophotonic Light Capture. *iScience*. **2018**; https://doi.org/10.1016/j.isci.2018.04.018.

21. Araújo A, Mendes MJ, Mateus T, et al. Ultra-fast plasmonic back reflectors production for light trapping in thin Si solar cells. *Sol Energy*. **2018**; https://doi.org/10.1016/j.solener.2018.08.068.

22. Haque S, Mendes MJ, Sanchez-Sobrado O, Águas H, Fortunato E, Martins R. Photonic-structured TiO2 for high-efficiency, flexible and stable Perovskite solar cells. *Nano Energy*. **2019**; https://doi.org/10.1016/j.nanoen.2019.02.023.

23. Mendes MJ, Haque S, Sanchez-Sobrado O, et al. Optimal-Enhanced Solar Cell Ultra-thinning with Broadband Nanophotonic Light Capture. *iScience*. **2018**; https://doi.org/10.1016/j.isci.2018.04.018.

24. Sanchez-Sobrado O, Mendes MJ, Haque S, et al. Colloidal-lithographed TiO2 photonic nanostructures for solar cell light trapping. *J Mater Chem C*. **2017**; https://doi.org/10.1039/c7tc01756a.

25. Yang Z, Gao P, Zhang C, Li X, Ye J. Scattering effect of the high-index dielectric nanospheres for high performance hydrogenated amorphous silicon thin-film solar cells. *Sci Rep*. **2016**; https://doi.org/10.1038/srep30503.

26. Schuster CS, Morawiec S, Mendes MJ, et al. Plasmonic and diffractive nanostructures for light trapping—an experimental comparison. *Optica*. **2015**; https://doi.org/10.1364/OPTICA.2.000194.

27. Morawiec S, Holovský J, Mendes MJ, et al. Experimental quantification of useful and parasitic absorption of light in plasmon-enhanced thin silicon films for solar cells application. *Sci Rep*. **2016**; https://doi.org/10.1038/srep22481.

28. Park KM, Lee MB, Choi SY. Investigation of surface features for 17.2% efficiency multi-crystalline silicon solar cells. *Sol Energy Mater Sol Cells*. **2015**; https://doi.org/10.1016/j.solmat.2014.07.023.

29. Yu KJ, Gao L, Park JS, et al. Light Trapping in Ultrathin Monocrystalline Silicon Solar Cells. *Adv Energy Mater*. **2013**; https://doi.org/10.1002/aenm.201300542.

30. Hong L, Yao H, Wu Z, et al. Eco-Compatible Solvent-Processed Organic Photovoltaic Cells with Over 16% Efficiency. *Adv Mater*. **2019**; https://doi.org/10.1002/adma.201903441.

31. Glinsner T, Lindner P, Mühlberger M, et al. Fabrication of 3D-photonic crystals via UV-nanoimprint lithography. Briones F, ed. *J Vac Sci Technol B Microelectron Nanom Struct*. **2007**; https://doi.org/10.1116/1.2798733.

32. Pourdavoud N, Wang S, Mayer A, et al. Photonic Nanostructures Patterned by Thermal Nanoimprint Directly into Organo-Metal Halide Perovskites. *Adv Mater*. **2017**;

https://doi.org/10.1002/adma.201605003.

33. Chou SY, Krauss PR, Renstrom PJ. Imprint Lithography with 25-Nanometer Resolution. Hosaka S, ed. *Science (80-)*. **2013**; https://doi.org/10.1126/science.272.5258.85.

34. Yu Y, Zhang G. Colloidal Lithography. In: Hosaka S, ed. *Updates in Advanced Lithography*. IntechOpen; **2013**; https://doi.org/10.5772/56576.

35. Chen J, Dong P, Di D, et al. Controllable fabrication of 2D colloidal-crystal films with polystyrene nanospheres of various diameters by spin-coating. *Appl Surf Sci*. **2013**; https://doi.org/10.1016/j.apsusc.2012.11.165.

36. Kohoutek T, Parchine M, Bardosova M, Fudouzi H, Pemble M. Large-area flexible colloidal photonic crystal film stickers for light trapping applications. *Opt Mater Express*. **2018**; https://doi.org/10.1364/OME.8.000960.

37. Kumar K, Kim Y-S, Yang E-H. The influence of thermal annealing to remove polymeric residue on the electronic doping and morphological characteristics of graphene. *Carbon N Y*. **2013**; https://doi.org/10.1016/j.carbon.2013.07.088.

38. Rizzato S, Primiceri E, Monteduro AG, et al. Interaction-tailored organization of large-area colloidal assemblies. *Beilstein J Nanotechnol*. **2018**; https://doi.org/10.3762/bjnano.9.150.

39. Akinoglu EM, Morfa AJ, Giersig M. Understanding Anisotropic Plasma Etching of Two-Dimensional Polystyrene Opals for Advanced Materials Fabrication. *Langmuir*. **2014**; https://doi.org/10.1021/la500003u.

40. Thangamuthu M, Santschi C, Martin OJF. Reliable Langmuir Blodgett colloidal masks for large area nanostructure realization. *Thin Solid Films*. **2020**; https://doi.org/10.1016/j.tsf.2020.138195.

41. Yang Y, Chu Y, Yang F, Zhang Y. Uniform hollow conductive polymer microspheres synthesized with the sulfonated polystyrene template. *Mater Chem Phys*. **2005**; https://doi.org/10.1016/j.matchemphys.2005.01.007.

42. Cai W, Wang W, Yang Y, Ren G, Chen T. Sulfonated polystyrene spheres as template for fabricating hollow compact silver spheres via silver–mirror reaction at low temperature. *RSC Adv*. **2014**; https://doi.org/10.1039/C3RA46210B.

43. Zhao K, Zhao J, Wu C, et al. Fabrication of silver-decorated sulfonated polystyrene microspheres for surface-enhanced Raman scattering and antibacterial applications. *RSC Adv*. **2015**; https://doi.org/10.1039/C5RA11643K.

44. Fujimura T, Tamura T, Itoh T, Haginoya C, Komori Y, Koda T. Morphology and photonic band structure modification of polystyrene particle layers by reactive ion etching. *Appl Phys Lett*. **2001**; https://doi.org/10.1063/1.1353844.

45. Ting Y, Liu C, Park S, Jiang H, Nealey PF, Wendt AE. Surface Roughening of Polystyrene and Poly(methylmethacrylate) in Ar/O2 Plasma Etching. *Polymers (Basel)*. **2010**; https://doi.org/10.3390/polym2040649.

46. Xia D, Ku Z, Li D, Brueck SRJ. Formation of Hierarchical Nanoparticle Pattern Arrays Using Colloidal Lithography and Two-Step Self-Assembly: Microspheres atop Nanospheres. *Chem Mater*. **2008**; https://doi.org/10.1021/cm702644c.

47. Amalathas AP, Alkaisi MM. Nanostructures for light trapping in thin film solar cells. *Micromachines*. **2019**; https://doi.org/10.3390/mi10090619.

48. Bozzola A, Liscidini M, Andreani LC. Photonic light-trapping versus Lambertian limits in

thin film silicon solar cells with 1D and 2D periodic patterns. *Prog Photovoltaics Res Appl*. **2012**; https://doi.org/10.1002/pip.1158.

49. Andreani LC, Bozzola A, Kowalczewski P, Liscidini M. Photonic light trapping and electrical transport in thin-film silicon solar cells. *Sol Energy Mater Sol Cells*. **2015**; https://doi.org/10.1016/j.solmat.2014.10.012.

50. Ingenito A, Isabella O, Zeman M. Opto-electronic evaluation of thin double-textured crystalline silicon wafers. *IEEE Int Conf Sustain Energy Technol*; **2013**; https://doi.org/10.1109/PVSC.2013.6744507.

51. Nayak PK, Mahesh S, Snaith HJ, Cahen D. Photovoltaic solar cell technologies: analysing the state of the art. *Nat Rev Mater*. **2019**; https://doi.org/10.1038/s41578-019-0097-0.

52. Smith Daivd D, Reich G, Baldrias M. et al. Silicon Solar Cells with total area efficiency above 25%. *IEEE 43rd Photovoltaic Specialist Conference (PVSC)*. **2016**; https://doi.org/10.1038/nenergy.2017.32.

53. Noppakuadrittidej P, Tonsomboon K, Ummartyotin S. Importance of solvent singularity on the formation of highly uniform hexagonal close packed (HCP) colloidal monolayers during spin coating. *Colloid Interface Sci Commun*. **2019**; https://doi.org/10.1016/j.colcom.2019.100177.

54. Almasi Kashi M, Ramazani A, Noormohammadi M, Zarei M, Marashi P. Optimum self-ordered nanopore arrays with 130–270 nm interpore distances formed by hard anodization in sulfuric/oxalic acid mixtures. *J Phys D Appl Phys*. **2007**; https://doi.org/10.1088/0022-3727/40/22/025.

55. Stępniowski WJ, Michalska-Domańska M, Norek M, Czujko T. Fast Fourier transform based arrangement analysis of poorly organized alumina nanopores formed via self-organized anodization in chromic acid. *Mater Lett*. **2014**; https://doi.org/10.1016/j.matlet.2013.11.099.

56. Chavez Boggio JM, Bodenmüller D, Fremberg T, et al. Dispersion engineered silicon nitride waveguides by geometrical and refractive-index optimization. *J Opt Soc Am B*. **2014**; https://doi.org/10.1364/JOSAB.31.002846.

57. Green MA. The Path to 25% Silicon Solar Cell Efficiency : History of Silicon Cell Evolution. *Prog Photovoltaics Res Appl*. 2009. https://doi.org/10.1002/pip.892

Appendices

A. Experimental

A.1 Polystyrene (PS) spheres preparation method

The method described below was performed to enable the polystyrene spheres' floatation in the air-liquid interface, self-assembly, and consequent monoarray formation since the original colloidal suspension contains water-soluble surfactants and salts that prevent them from float:[40]

1) 98.9 μL of diacetone was pipped out to a 2 ml Eppendorf tube.
2) 1,0 μL of styrene (≥ 99 %) was added, followed by the addition of 0.1 μL of concentrated sulfuric acid (98 %) and mixed for 1 minute in an MS-X Vortex Mixer.
3) 100 μL of the original suspension was added, totaling **200 μL**, followed by 1-minute agitation.

It is worth noting that, for the simultaneous deposition of this colloidal mask 2 in wafers, ~400 μL of this suspension was needed.

A.2 Langmuir-Blodgett (LB) deposition method

The following method was performed in every deposition:

1) Before filling the trough with 700 ml of deionized water (DI), it was cleaned with DI and EtOH.
2) A laboratory aspirator was used to remove impurities and air bubbles from the resultant DI bed.
3) The dipper zero was set when the substrate was slightly above the air-water interface. This position constitutes the final position of the dipped substrate.
4) After a complete dip, a slow dropping of ~400 μL of the previous dispersion onto the interface with a microsyringe was performed.
5) Both barriers were initially closed with a controlled compression velocity of 5 mm/min, which led the polystyrene spheres to form the close-packed hexagonal monoarray on the same interface.
6) Then, their vertical withdrawal at a compression velocity of 4 mm/min leads to the complete transfer of the ordered monoarray to the wafers' surface, while the barriers close at the same speed, to preserve the film arrangement.[40]

When the withdrawal is initiated, it is worth noting that the remaining closure distance of the barriers must be equal to or higher than the substrates' length to cover the substrates completely.

A.3 Colloidal mask shaping, infiltration, and rear mirror deposition

Table SA1. Applied experimental conditions throughout the two distinct dry etching (reactive ion etching, RIE) time procedures.

RIE gas	Etched Material	Time (s)	RIE Power (W)	Gas Pressure (mTorr)	Gas Flow (sccm)
O_2	Polystyrene	100, 200, 250 300, 350, 400	50	50	50
Ar/CF_4	TiO_2	90	100	100	4/16

Table SA2. Applied experimental conditions throughout the radio frequency (RF) sputtering (infiltration) processes.

Material	O_2 gas pressure (mbar)	Ar gas pressure (mbar)	Power (W)	Deposition rate (nm min^{-1})	Distance to sample (cm)	Pre-sputtering time (min)	Target specifications
TiO_2	10^{-5}	2×10^{-3}	200	2.5	15	15	TiO_2 99.99 % purity, 3 in diameter

Table SA3. Applied experimental conditions throughout the resistive thermal evaporation (rear mirror deposition) procedures.

Crucible	Evaporated Material	Current (A)	Vacuum (mbar)	Deposition rate (nm s^{-1})	Distance to sample (cm)	Evaporated material specifications
Mo	Ag	128	10^{-6}	0.3	10	Ag 99.99 % purity

Mo, Molybdenum

Table SA4. Summary of O_2 reactive ion etching (RIE) exposition times, TiO_2 targeted, and simulated (underlined) light trapping (LT) for each respective wafer (conventional 250 μm and thin 90 μm crystalline silicon, c-Si, wafers).

Substrate	RIE time (s)	TiO_2 Targeted // <u>Simulated</u> LT structures thickness (nm)
250 μm c-Si wafer	100	200 // <u>260</u>
		400 // <u>325</u>
		700 // <u>757</u>
	200	200 // <u>260</u>
		400 // <u>325</u>
		700 // <u>757</u>
	300	200 // <u>290</u>
		400 // <u>430</u>
		700 // <u>792</u>
	400	200 // <u>290</u>
		400 // <u>511</u>
90 μm c-Si wafer	250	450 // <u>410</u>
		500 // <u>527</u>
		700 // <u>693</u>
	300	450 // <u>405</u>
		500 // <u>525</u>
		700 // <u>693</u>
	350	450 // <u>405</u>
		500 // <u>525</u>
		700 // <u>693</u>

Table SA5. Summary of O_2 reactive ion etching (RIE) exposition times, TiO_2 target, and simulated (underlined) light trapping (LT) for each solar cell here engineered (textured, etched, and flat interdigitated back contact solar cells with 130, 140, and 740 μm crystalline silicon thicknesses, respectively).

Sample (IBCSC)	**RIE time (s)**	**TiO_2 Targeted // <u>Simulated</u> LT structures thickness (nm)**
Textured (130 μm)	100	200 // <u>266</u>
		400 // <u>530</u>
		600 // <u>726</u>
	200	200 // <u>266</u>
		400 // <u>530</u>
		600 // <u>726</u>
	300	200 // <u>266</u>
		400 // <u>530</u>
		600 // <u>726</u>
	400	200 // <u>266</u>
		400 // <u>530</u>
		600 // <u>726</u>
Etched (140 μm c-Si)	300	200 // <u>281</u>
		300 // <u>423</u>
		400 // <u>448</u>
		500 // <u>545</u>
		800 // <u>885</u>
Flat (740 μm c-Si)	300	500 // <u>456</u>
		800 // <u>874</u>

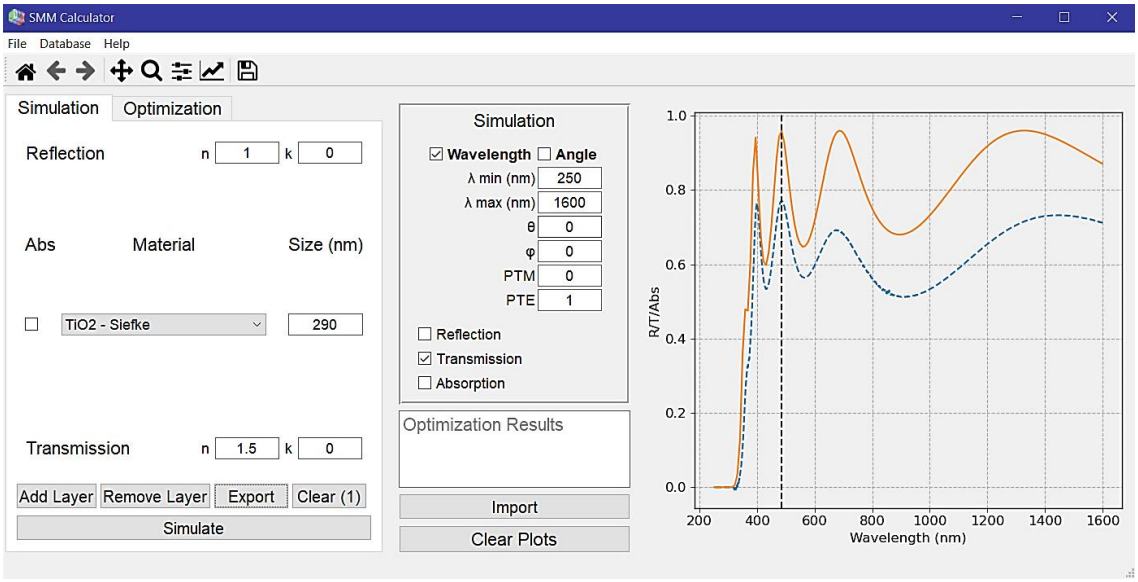

Figure SA1. Simulation interface (Scatmm) used to determine the resultant TiO_2 film thickness deposited on glass through scattering matrix method. The simulated data for the inserted thickness (290 nm) in full orange line is compared with original transmittance data (dashed blue line), considering the $n(\lambda)$ and $k(\lambda)$ (real and imaginary part, respectively) of TiO_2 from Siefke. The real part of the glass refractive index (underneath layer) is indicated. Since the peaks of the original data are the most aligned possible with the simulation data (see vertical dash black line), it is concluded that the deposited TiO_2 thickness is equal to 290 nm. More information can be found in: *https://bit.ly/3RUI28J1.* The vertical mismatch between the simulated and measured spectra is mainly related with parasitic absorption in the thick glass substrate.

B. Results and Discussion (Complementary)

B.1 Fast Fourier Transform (FFT) and Voronoi Diagrams

It is essential to understand the practical significance of FFT imagery and Voronoi diagrams. Briefly, FFT comprises a graphical depiction of a grayscale image (as attained with scanning electron microscopy, SEM) in terms of its structure ordering. It establishes a distance relation between a center element and its surroundings, allowing for qualitative analysis. A highly ordered array should correspond to an FFT image where clear and bright peaks are shown, being related with a hexagonal shape or honeycomb structure, and, oppositely, an unordered array should correspond to fading concentrical rings (see Figure SB1A and B, respectively). These rings are related to periodicity throughout the analyzed area, where a higher number of reasonably focused concentric rings or bright peaks correspond to a more extensive periodicity. The structural homogeneity is also assessed but more intuitively by Voronoi diagrams, where a binary representation of the original image is shown.[53–55]

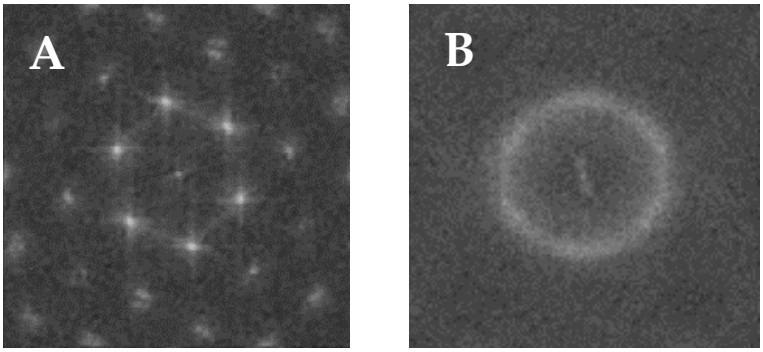

Figure SB1. FFT images representing a (**A**) highly ordered (**B**) unordered PS spheres array. A more hexagonal shape formed by the peaks (bright dots) is due to a more hexagonally ordered array (more similar to a honeycomb structure). [40]

After obtaining the FFT images, it is possible to apply to them a Radial Profile distribution function (performed with *ImageJ* plugin Radial Profile Plot), plotting the normalized integrated intensity as a function of the spheres' diameter.[2] It is then possible to assess the resulting array order and periodicity quantitatively. Practically, it is used to number the distinguishable FFT imagery rings.[53]

B.2 Photonic nanostructured coatings characterization

B.2.1 Conventional (250 μm) c-Si wafers

B.2.1.1 Morphological and optical assessment

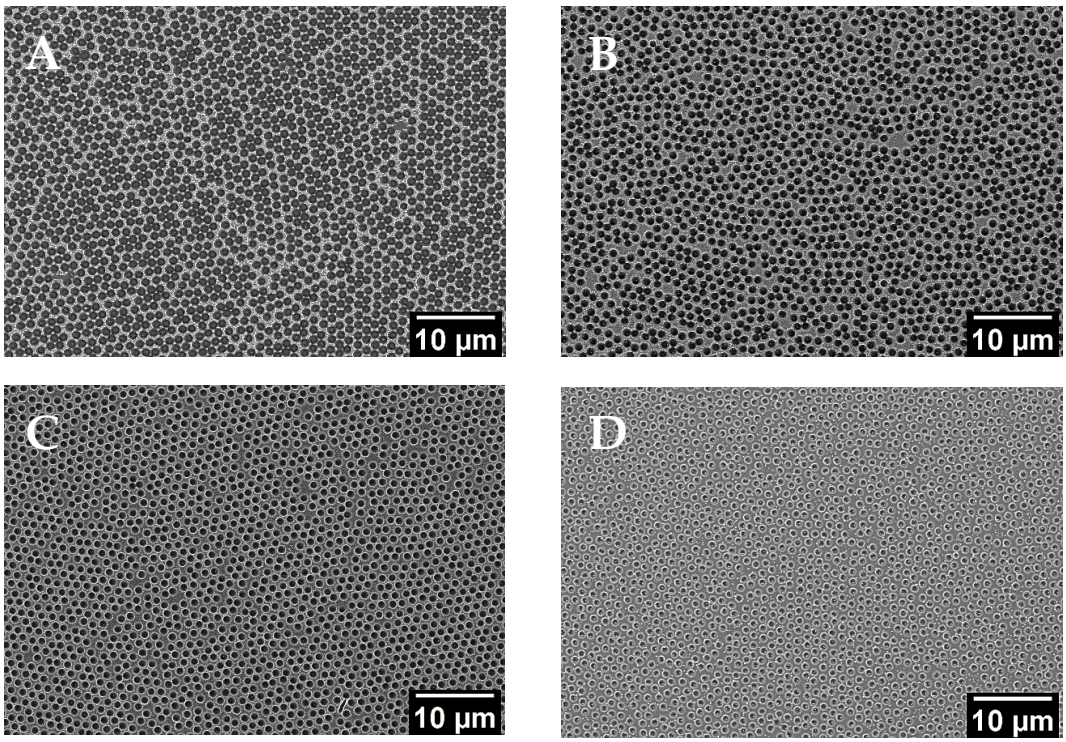

Figure SB2. Low magnification scanning electron microscopy (SEM) imagery of top view of photonic voids array with respect to the 200 nm TiO_2 (simulated thickness of 275 ± 15 nm) batch, where each colloidal mask was submitted to (**A**) 100, (**B**) 200, (**C**) 300 and (**D**) 400 s of O_2 reactive ion etching time, t_{RIE}.

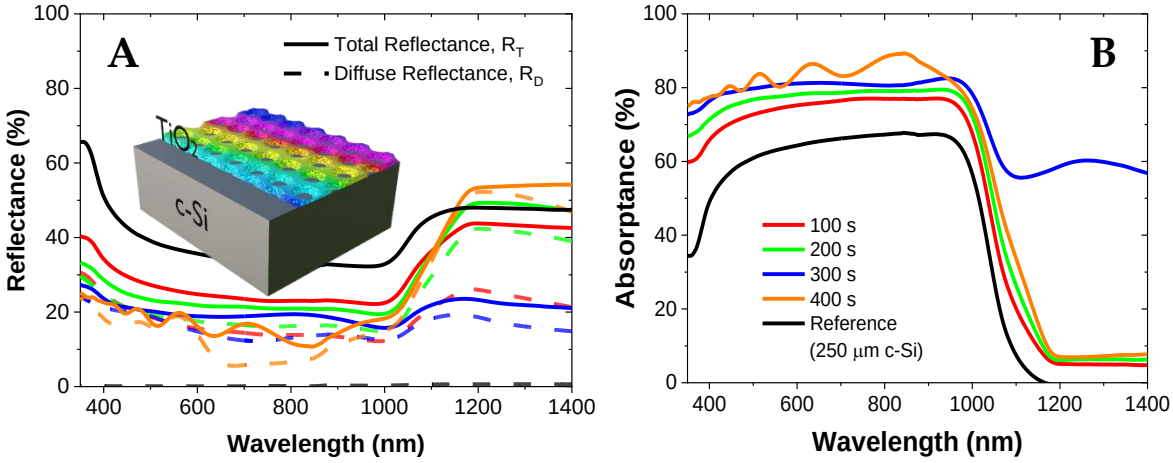

Figure SB3. Complementary total and diffuse (full and dash line, respectively) (**A**) reflectance and (**B**) calculated absorptance spectra for the conventional (250 μm) c-Si wafers coated with photonic nanostructured coatings resultant from O_2 reactive ion etching time equal to 100 (red), 200 (green), 300 (blue) and 400 (orange) seconds. Simulated thicknesses are respectively the following: 325 (100 and 200 s), 430 (300 s) and 511 (400 s) nm of TiO_2. In black, optical performance of reference (uncoated flat wafer).

B.2.1.2 Topographical assessment

The top-view morphology measured via Atomic Force Microscopy (AFM) of the TiO_2 photonic nanostructured coatings of the best-performing samples (in terms of average absorption, $\langle Abs \rangle$, and photocurrent density, J_{ph}) is presented in Figure S1. It was possible to correlate the structures' average height with the equivalent (simulated) TiO_2 film thickness. The average heights that induce a higher $\langle Abs \rangle$ or J_{ph} are respectively the following: (A) 0.429 ± 0.070 and (B) 0.669 ± 0.055 μm.

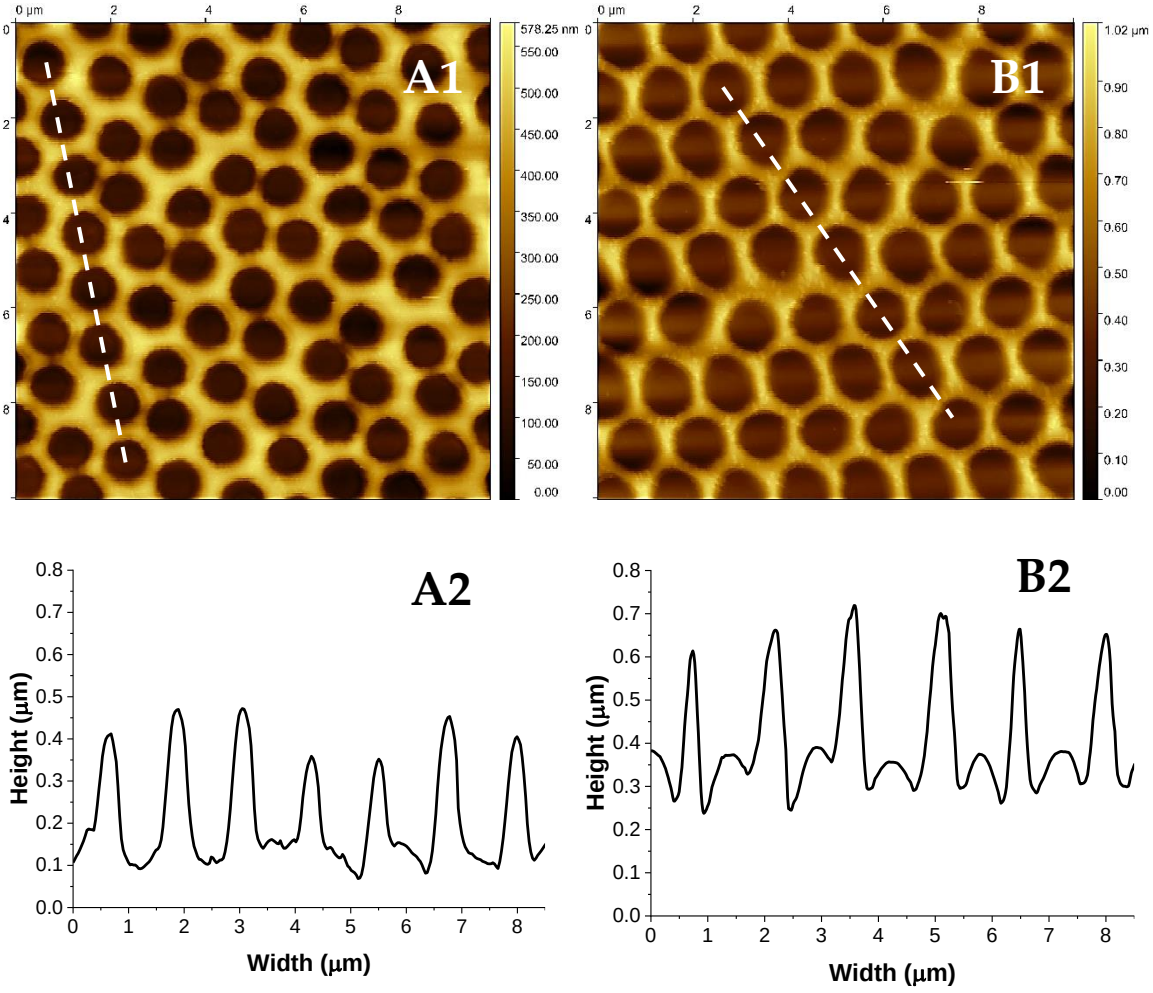

Figure SB4. Atomic Force Microscopy (AFM) top-views of the two designs on thick (250 μm) c-Si wafer with the highest average absorption and photocurrent density, respectively: (**A1**) simulated thickness of 430 nm TiO_2, with obtained average height of TiO_2 0.429 ± 0.070 nm, which was determined using the data from (**A2**) height profile correspondent to the dashed line in A1; (**B1**) simulated thickness of 793 nm TiO_2, with obtained average height of TiO_2 0.669 ± 0.055 nm, determined using the data from (**B2**) height profile correspondent to the dashed line in B1. Both are resultant of 300 seconds of RIE (O_2) time.

B.2.2 Thin (90 μm) c-Si wafers

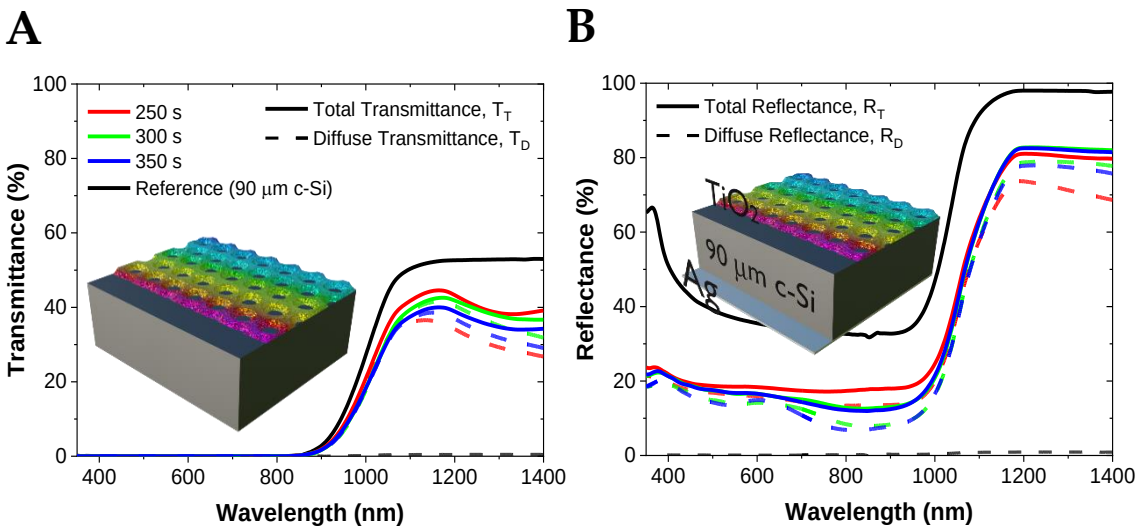

Figure SB5. (**A**) Transmittance spectrum concerning 90 μm flat c-Si wafers coated with photonic nanostructures with the targeted thickness of 700 nm of TiO_2 (respective 693 nm of simulated thickness) for the various O_2 reactive ion etching times, t_{RIE}: 250, 300 and 350 seconds. In (**B**) the reflectance spectra regarding the previous specifications but where ~300 nm of Ag rear mirrors were applied. Respective references (in black) correspond to (A) a single thin c-Si wafer and (B) with a Ag rear mirror.

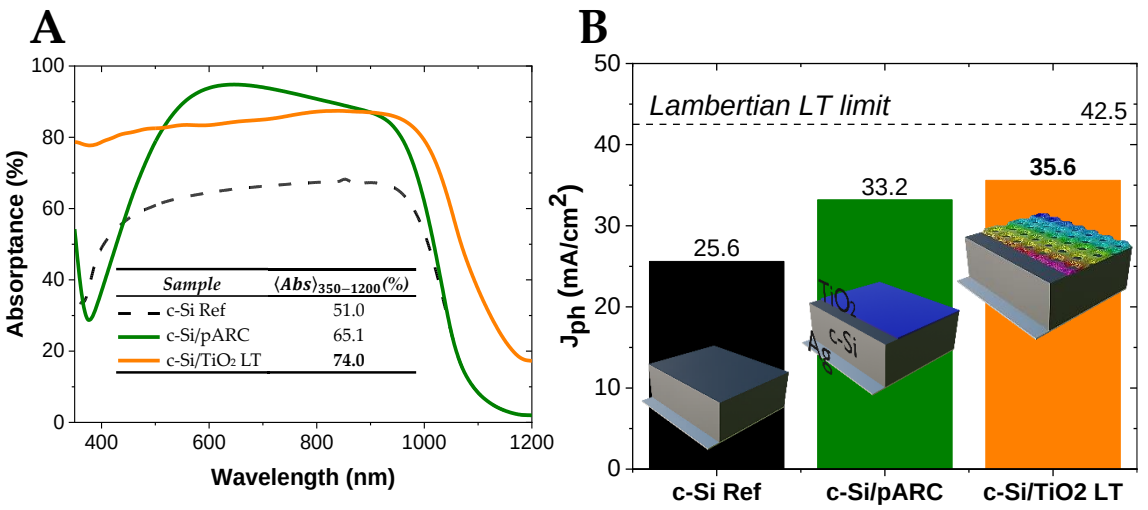

Figure SB6 (**A**) Absorptance spectra of a flat silicon wafer (reference, c-Si reference in black), a coated wafer of 90 μm c-Si thickness with ~50 nm of TiO_2 (optimized planar antireflection coating, c-Si/pARC, in green) or with light trapping (LT) nanovoid array (c-Si/TiO_2 LT, correspondent to 693 nm TiO_2 of simulated thickness, 300 s of reactive ion etching time orange, respectively. (**B**) Spectrally integrated (350-1200 nm) absorptance, presented regarding photocurrent density J_{ph} determined as described in this work for the three samples analyzed in (A) and whose architecture is sketched on top of each bar. The determined J_{ph} of theoretical geometrical optics case of the respective Lambertian LT limit (90 μm of c-Si) is marked with a horizontal dashed line in (B).

B.2.3 Photonic coatings on etched Interdigitated Back Contact Solar Cells (IBCSCs)

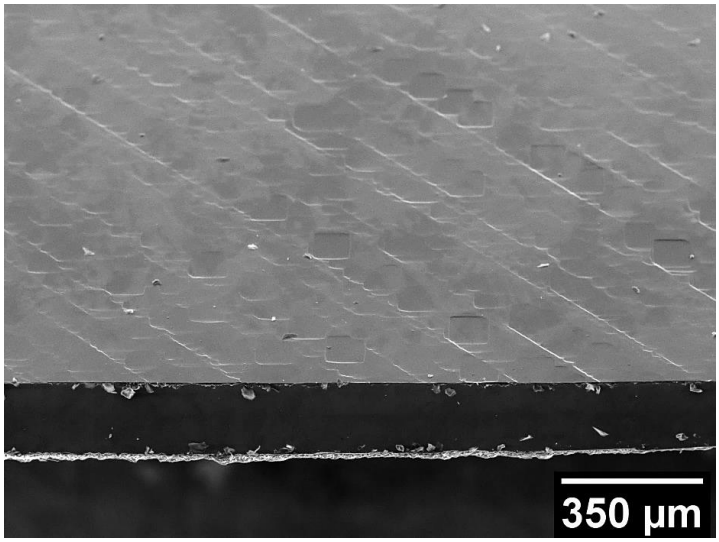

Figure SB7. Scanning electron microscopy transversal image of a previously cutted pristine etched interdigitated back contact solar cell (IBCSC), where the microscale roughness, result of an original alkaline etching on the front side, is observed.

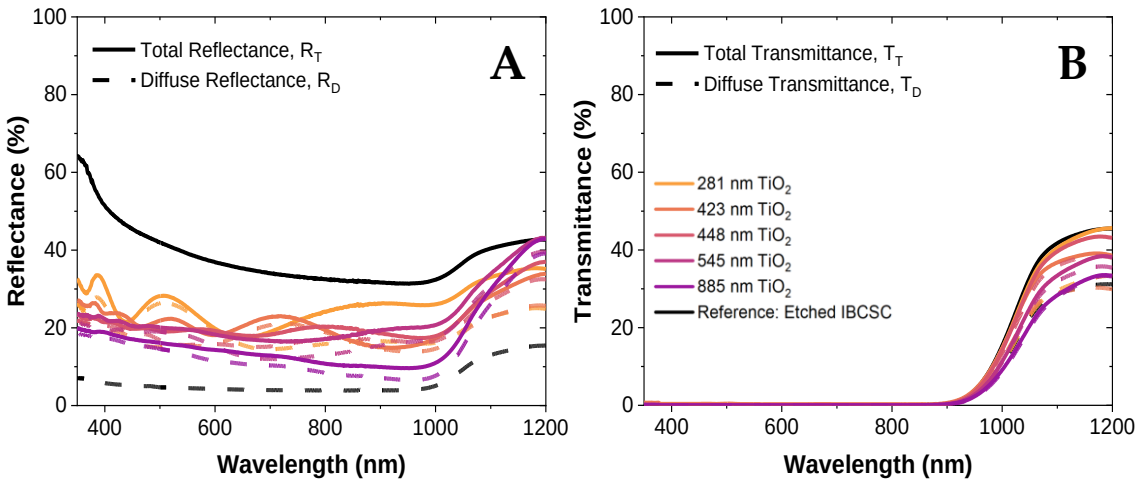

Figure SB8. (**A**) Reflectance and (**B**) transmittance spectra of etched interdigitated back contact solar cell coated with photonic nanostructures for the different TiO_2 thicknesses: 281, 423, 448, 545 and 885 nm. Commonly, O_2 t_{RIE} = 300 s.

B.2.4 Photonic coatings on flat IBCSCs

A similar colloidal lithography process was applied on thick (740 μm of crystalline silicon, c-Si, absorber) flat IBCSC, maintaining the O_2 RIE time, t_{RIE}, (300 seconds) and varying the TiO_2 infiltration thickness (456 and 874 nm). Figure SB9 presents the top view of the resulting photonic TiO_2 nanostructured coating on a flat IBCSC (fIBCSC), respectively with 874 nm of TiO_2. Not only are the voids distinguishable from the underneath layer (c-Si active layer in black in the center of each void), but they are also highly arranged.

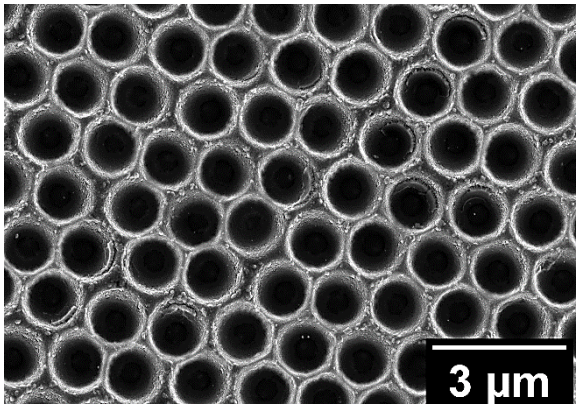

Figure SB9. SEM image of the top view of photonic voids array concerning the 874 nm TiO_2 batch, submitted to 300 seconds of O_2 t_{RIE}, directly engineered on top of a flat (polished) IBCSC absorber layer (c-Si).

These coatings determine the optical performance of the coated IBCSCs. Oppositely to the obtained so far, these wavelength-sized features do not increase the light scattering when applied in such thick absorbers, as shown in Figure SB10A. In this case, only the anti-reflection effect provides optical benefits, specifically in a broad wavelength range (UV-VIS-NIR), as observed in Figure SB10B. Thus, a broad absorption enhancement (see Figure SB10C) relative to the uncoated fIBCSC reference is attained. Consequently, a substantial average absorption $\langle Abs \rangle$ between 350 and 1200 nm is attained: more than 77 and 81 % for 456 and 874 nm of TiO_2, respectively, when the reference (uncoated fIBCSC, in black) only reached 70 % (see inset of Figure SB10C). This corresponds to respective average absorption enhancements of ~11 and 17 % concerning the uncoated fIBCSC. As such, further electrical measurements should be considered to thoroughly analyze the impact of the designed coatings on the thick (740 μm) flat interdigitated back contact solar cells.

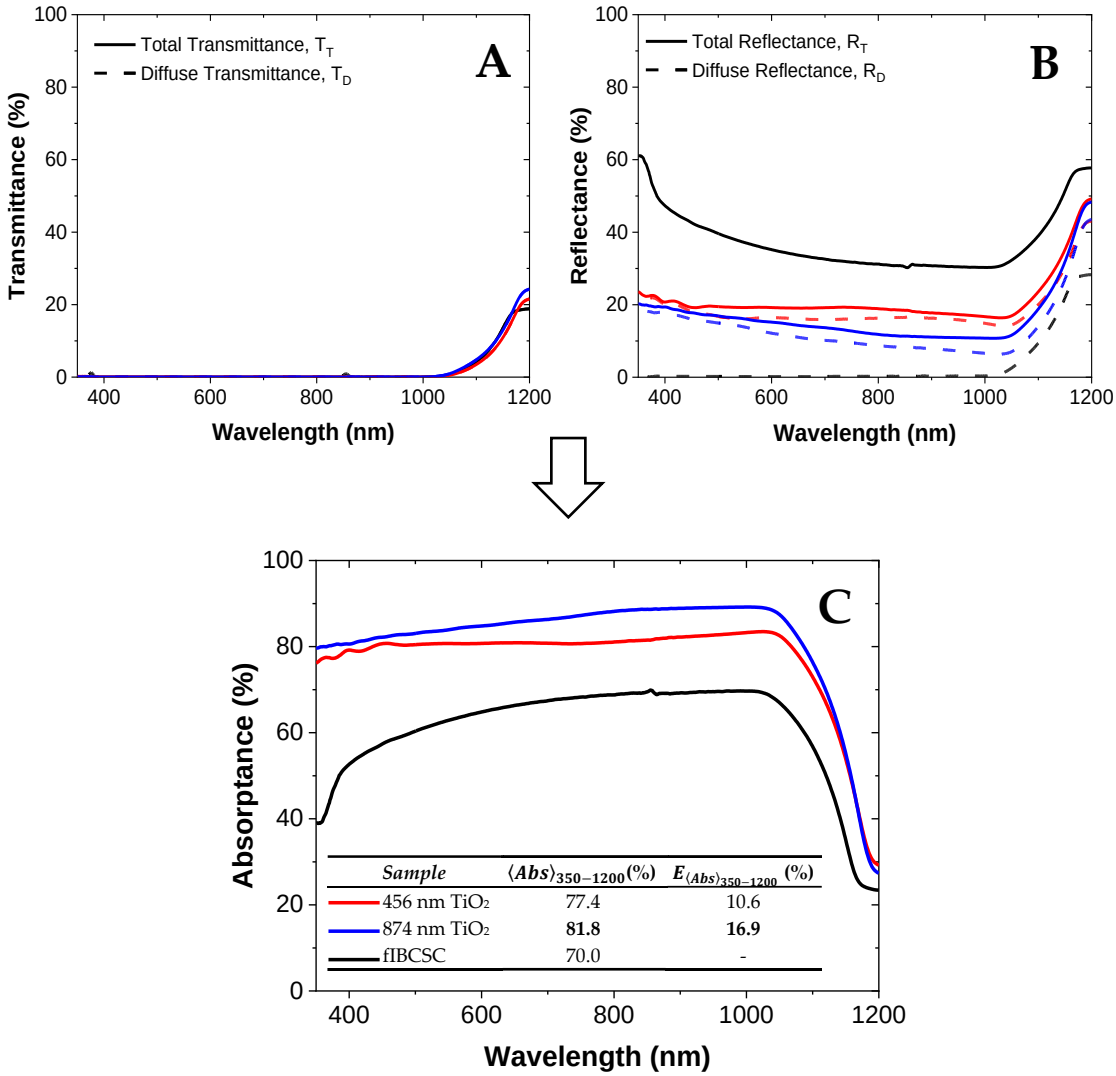

Figure SB10. (**A**) Measured reflectance, (**B**) transmittance (total in full and diffuse in dashed lines) and (**C**) calculated absorptance spectra of flat IBCSCs (740 µm c-Si) coated with photonic nanostructures for the different TiO_2 thicknesses: 456 (red) and 874 (blue) nm of TiO_2. Commonly, $t_{RIE} = 300$ s. These are compared to the optical performance of the uncoated reference IBCSC (in black). Respective average absorption values determined between 350 and 1200 nm are presented in inset of (C).

B.2.5 Photonic coatings on textured IBCSCs

Pre-diced textured interdigitated back-contact solar cells (tIBCSC) samples (originally coated with a silicon nitride optimized anti-reflection coating) were also submitted to a similar colloidal lithography procedure as described in subsection 3.1. In this case, the O_2 t_{RIE} took the following values 100, 200, 300, and 400 seconds. TiO_2 was deposited with the targeted thicknesses of 200, 400, and 600 nm (see Table SA5, Appendix A, section 3 for all simulated thicknesses). These coatings were engineered on top of the inherent texture of the original tIBCSCs shown in Figure SB12A. Respectively in Figure SB12B and the topographical projection of Figure SB12C, the voids are not as well defined as observed on flat wafers. Despite that, it is possible to distinguish both types of features.

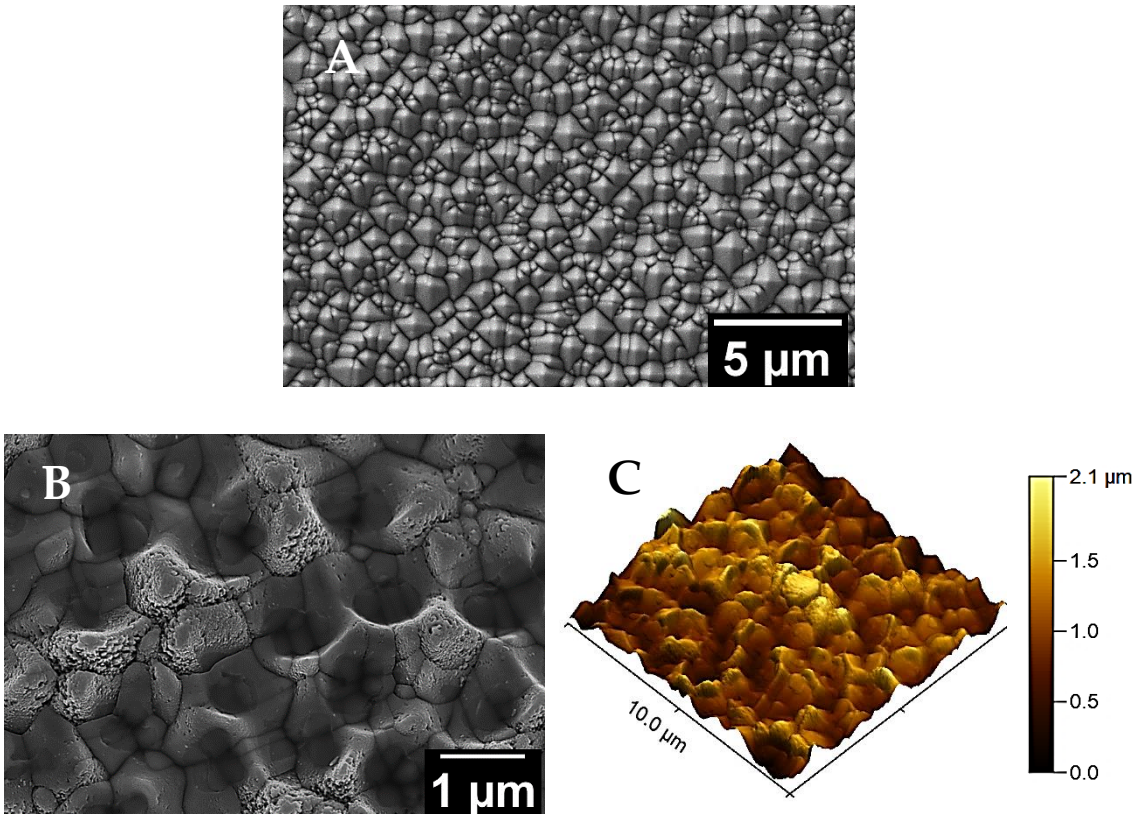

Figure SB11. (**A**) SEM top-view of pristine and (**B**) photonic nanostructured IBCSCs (726 nm TiO_2, t_{RIE} = 100 s), and (**C**) 3D orthographic projection of AFM of 10×10 µm² top-view. Respective scales are also presented.

The inherent textures of these solar cells translate into an optimized absorption in the Visible range (350-750 nm), where the solar spectral irradiance is greater, and in lower near-infrared (NIR) wavelengths (750-1000 nm), as seen in Figure SB12A, where ~100 % of the incident photons are absorbed. However, these structures do not interact with Ultraviolet (UV) photons as efficiently as their combination with the designed

voids. This combination doubles the absorption in the UV range attained by the original pyramidal textured, now exceeding ~95 % and which is more significant for O_2 t_{RIE} = 400 s (yellow line), due to the more intense anti-reflection effect provided by the applied coating, as seen in Figure SB12B in that range. Contrastingly, the optimized optical response of the original features in the Visible surpasses the attained by the combination of distinct structures. Additionally, the same sample led to the highest decrease in absorption in the Visible band and lower NIR wavelengths, as observed for the remaining samples.

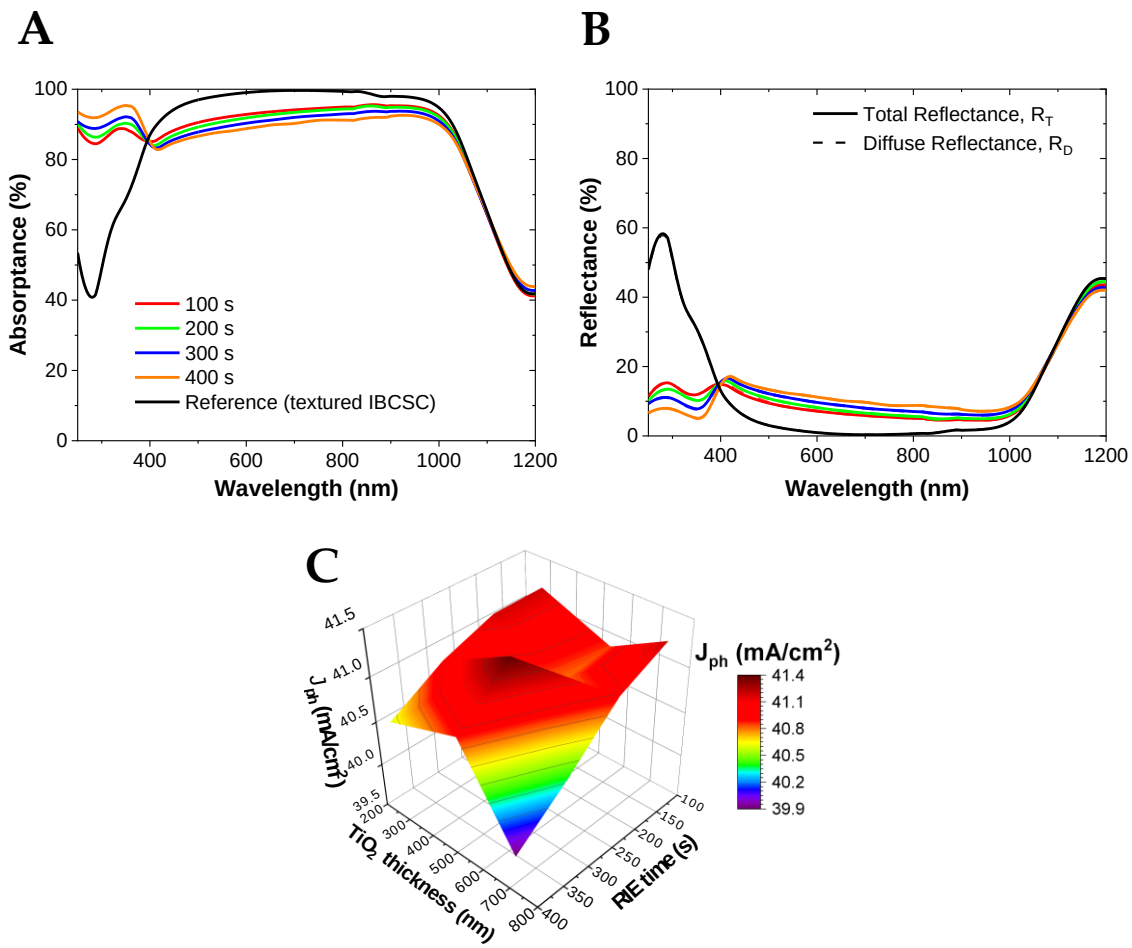

Figure SB12. **(A)** Absorptance and (**B**) reflectance (total and diffuse) spectra for textured IBCSCs covered with the photonic coatings with simulated TiO_2 thickness of 726 nm submitted to the O_2 t_{RIE} = 100 (red), 200 (green), 300 (blue) and 400 (orange) seconds (O_2). In black, optical performance of reference (pristine textured IBCSC) is presented. (**C**) 3D plot of photocurrent density is also presented, in terms of its evolution in terms of TiO_2 thickness (simulated) and t_{RIE}.

To evaluate the electrical performance of the nanostructured texturized samples, the experimental conditions which resulted in the best optical performance were selected among all batches. Thus, the respective photocurrent density (J_{ph}) values,

which were determined similarly to the previous sections, are presented in the 3D plot of Figure SB12C. The selected samples and the maximum respective attained J_{ph} values are presented in Table SB1.

Table SB1. Selected experimental conditions (TiO_2 thickness and O_2 t_{RIE}) in terms of maximum calculated J_{ph}, to apply on cutted tIBCSCs to submit to electrical measurements.

TiO_2 thickness (nm)	**RIE time (s)**	**J_{ph}(mA/cm²)**
266	100	41.2
	200	
726	100	

When applied on tIBCSCs, the here-designed photonic structures do not enhance their electrical performance, as seen curves for all wavelengths in the external quantum efficiency (EQE) presented in Figure SB13A. And as seen in Figure SB13B, the best performing sample (266 nm TiO_2, 100 s O_2 RIE time) showed ~13 % of PCE, diminishing the pristine PCE (~15 %) in ~14 %. This is due to the contribution of several factors. Firstly, the void features applied on top of the original micrometric pyramidal textures diminish the already optimized optical performance of these last ones. By interacting first with light, the superior broadband absorption effect is verified. Therefore, the observed reduction in EQE in the Visible range, caused by the reflection heightening in the same range, led to efficiency diminishment. Secondly, the engineered voids are not applied directly on top of the active layer. This may lead to parasitic absorption in the underneath layer (anti-reflection coating composed of silicon nitride, Si_3N_4) and/or in the nanostructured coating for low wavelengths (< 480 nm). Third and lastly, the selected material to compose the designed features is not the most appropriate, as it should also contribute to a gradually varying effective refractive index matching, which is not the case, as n_{TiO_2}~2.5-2.7 and $n_{Si_3N_4}$~1.7-2.2[56]. As such, using other materials with a relatively high-real part of their refractive index but that present a closer high-real part of its refractive index to the underneath silicon nitride layer, as ZnO-based TCOs (e.g., AZO, n~1.8-2), is more suitable to apply over typical anti-reflection coatings (including SiO_2, since n_{SiO_2}~1.8-2.2[57]). The correspondent J-V curves, short-circuit current density

(J_{sc}) and open circuit voltage (V_{oc}) values are presented in Figure SB13B-C and Table SB2, respectively.

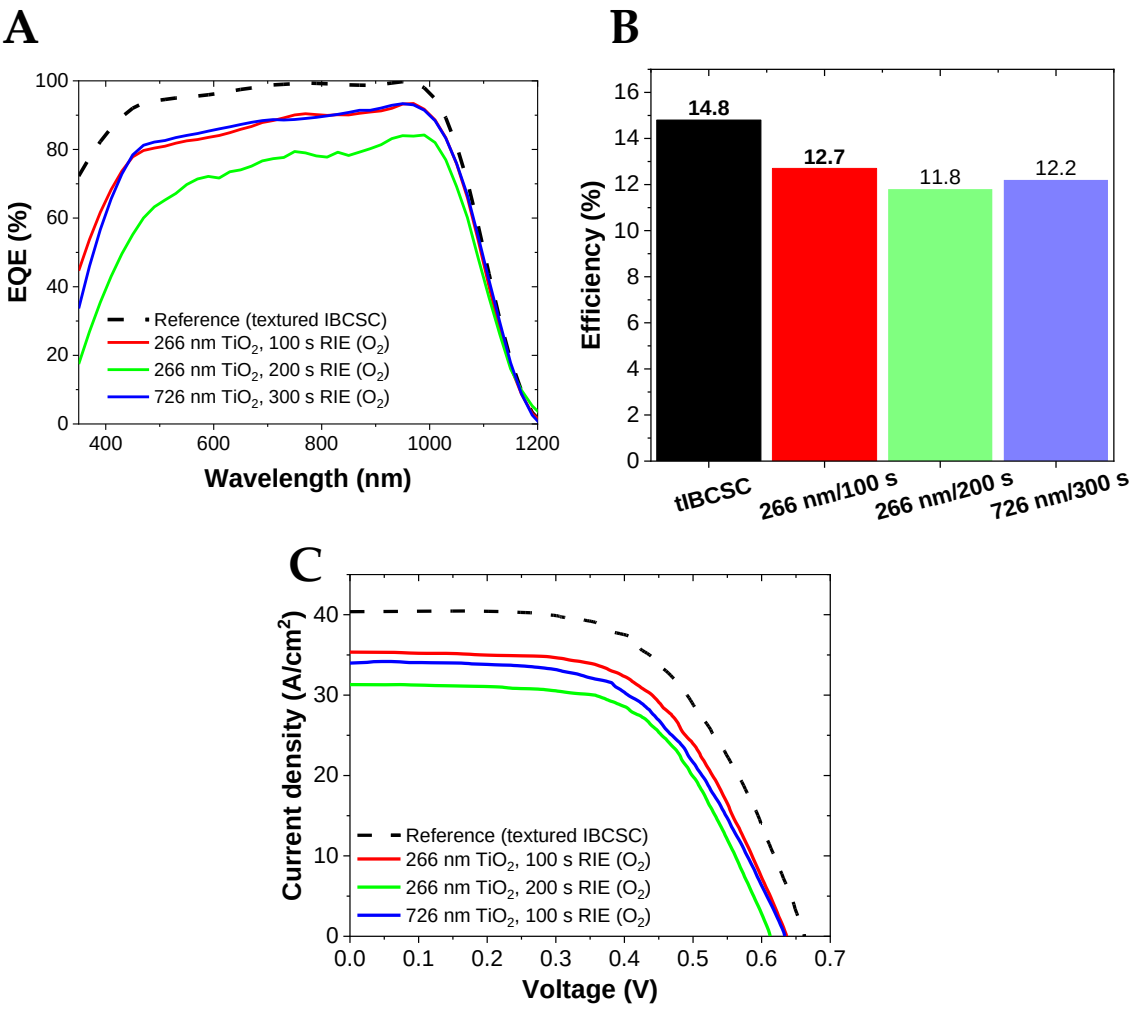

Figure SB13. (**A**) External quantum efficiency (**B**) power conversion efficiency (PCE), for the designed cells indicated in Table SB2 with distinct TiO_2 thickness and/or O_2 t_{RIE}. Respective (**C**) J-V curves, as for the considered original tIBCSC reference in black (bars and dashed lines).

Table SB2. J_{sc} and V_{oc} values respective to the best-performing designed textured cells indicated in Table SB1.

Sample	J_{sc} *(mA/cm²)*	V_{oc} *(V)*
Textured IBCSC	40.4	0.66
266 nm TiO_2, 100 s RIE (O_2)	35.4	0.63
266 nm TiO_2, 200 s RIE (O_2)	31.3	0.61
200 nm TiO_2, 100 s RIE (O_2)	34.0	0.63